INVESTIGATION OF AEROSOL EFFECTS ON THE ARCTIC SURFACE TEMPERATURE

DURING THE DIURNAL CYCLE

by

Eric Stofferahn

A Dissertation
Submitted to the
Graduate Faculty
of
George Mason University
In Partial fulfillment of
The Requirements for the Degree
of
Doctor of Philosophy
Climate Dynamics

Committee:

_____	Dr. Zafer Boybeyi, Dissertation Director
_____	Dr. James Kinter, Committee Member
_____	Dr. Timothy DelSole, Committee Member
_____	Dr. Michael Summers, Committee Member
_____	Dr. Paul Schopf, Department Chair
_____	Dr. Donna M. Fox, Associate Dean, Office of Student Affairs & Special Programs, College of Science
_____	Dr. Peggy Agouris, Dean, College of Science

Date: _____ Spring Semester 2015
George Mason University
Fairfax, VA

Investigation of Aerosol Effects on the Arctic Surface Temperature during the Diurnal Cycle

A dissertation submitted in partial fulfillment of the requirements for the degree of Doctor of Philosophy at George Mason University

By

Eric Stofferahn
Master of Science
George Mason University, 2008
Bachelor of Science
James Madison University, 2005

Director: Dr. Zafer Boybeyi, Professor
Department of Atmospheric, Oceanic, and Earth Sciences

Spring Semester 2015
George Mason University
Fairfax, VA

Dedication

I dedicate this dissertation to my wife Shannon, whose unwavering support has meant everything to me.

Acknowledgments

I would like to thank the many people who have made this dissertation possible. Dr. Zafer Boybeyi was an invaluable advisor. Dr. Timothy DelSole, Dr. James Kinter, and Dr. Michael Summers have each helped immensely on this project and I thank them all for being on my committee. Dr. Vladimir Alexeev, IARC, and the members of the NABOS Expedition of 2013 allowed me to see the Arctic in person. Additional thanks to the Department of Energy, the National Science Foundation, and the National Center for Atmospheric Research for access to computational resources and expertise.

Table of Contents

List of Tables

List of Figures

Abstract

INVESTIGATION OF AEROSOL EFFECTS ON THE ARCTIC SURFACE TEMPERATURE DURING THE DIURNAL CYCLE

Eric Stofferahn, PhD

George Mason University, 2015

Dissertation Director: Dr. Zafer Boybeyi

Temperature changes in the Arctic due to anthropogenic climate change are larger in magnitude than those at lower latitudes, with sea ice extent and thickness diminishing since the dawn of the satellite era. Aerosols may play a vital role in determining the changes to the Arctic. Specifically, the ability of absorbing aerosols to change the vertical structure of the atmosphere and sulfate aerosols to act as cloud condensation nuclei play important parts in the maintenance of Arctic stratiform clouds. However, there are still large uncertainties in the impact of aerosols on the changes in Arctic surface temperature, particularly during the diurnal cycle.

This study attempts to address these changes using the Weather, Research, and Forecasting Chemistry (WRF-CHEM) model. The study investigates the changes in surface temperature, as well as the variables which affect surface temperature, due to aerosol effects in the Arctic. A suite of ensemble runs are used to develop a filtering mechanism based upon the t-test to eliminate the effects of meteorological variability. The total aerosol effect is then separated into the changes caused by the aerosol direct effect, the aerosol semi-direct effect, and the aerosol indirect effects through the use of additional WRF-CHEM runs. The study shows that aerosol indirect effects are the dominant influence on surface temperature changes throughout the diurnal cycle. While much has been speculated about the cooling role of indirect aerosol effects, this study shows that the indirect effects have both a warming and cooling effect, depending upon the time of day, underlying surface properties, and aerosol size distribution/concentration.

Chapter 1: Introduction

1.1 Climate Change

Over the past few decades, international concern has grown about anthropogenic climate change. The surface temperature of the globe has warmed by 0.85 K since 1880 (Hartmann et al., 2013) and much of this warming has been attributed to the release of greenhouse gases (Hartmann et al., 2013; Myhre et al., 2013), which affects the surface temperature through changes in radiative forcing. Climate projections indicate that these changes would be accompanied by a *very likely* rise in sea level, *likely* changes in precipitation patterns (mainly in land areas), and the possibility of increased floods and droughts (Cubasch et al., 2013). Still, there are uncertainties associated with the projected temperature increases. While uncertainty in future emissions (particularly of greenhouse gases) remains the primary obstacle to a precise prediction, gaps in scientific understanding of the impact of clouds and aerosols on radiative forcing present an additional challenge. The objective (Section 1.4) of this study seek to address these gaps.

1.1.1 Temperature

It is certain that globally averaged land-surface air temperature has risen since the late 19th century and that this warming has been particularly marked since the 1970s (Hartmann et al., 2013) (Fig. 1.1). In addition, sea surface temperatures (SSTs) have increased globally since the 1950s and since the late 19th century (Hartmann et al., 2013) (Fig. 1.2). Each of the past three decades has been warmer than all the previous decades in the instrumental record, and the decade of the 2000s has been the warmest. When taken as a combined land and ocean surface temperature and globally averaged, there is a warming of 0.85 [0.65

to 1.06] °C over the period from 1880-2012, though substantial decadal and inter-annual variability exists within this time-frame (Hartmann et al., 2013).

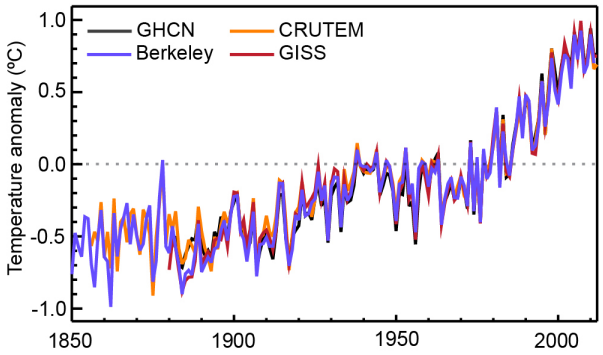

Figure 1.1: Global Annual Average Land-Surface Air Temperature Anomalies Relative to a 1961-1990 Climatology from 4 reanalyses (Hartmann et al., 2013).

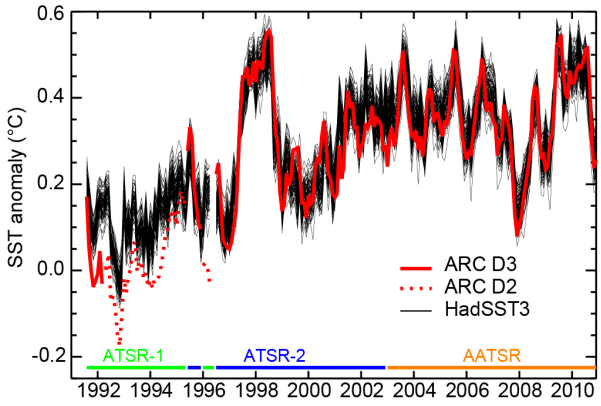

Figure 1.2: Global Monthly Mean Sea Surface Temperature (SST) Anomalies Relative to a 1961-1990 Climatology from Satellites (ATSRs) and *in situ* records (HadSST3) (Hartmann et al., 2013).

The warming of the past century has not been uniform. There is variability in the change of surface temperature from region to region (note the Arctic). However, it is accurate to say that a large portion of the globe has experienced surface warming during this period

(Fig. 1.3).

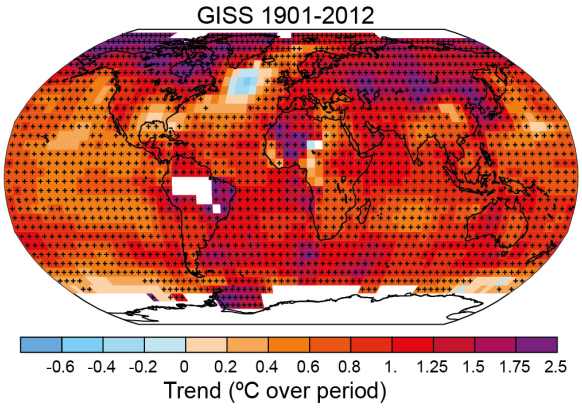

Figure 1.3: Map of Trends in Surface Temperature for 1901-2012 from GISS (some interpolation involved) (Hartmann et al., 2013). Note the large warming in the Arctic.

Projections of surface temperature changes are based largely on models involved in the Coupled Model Intercomparison Project Phase 5 (CMIP5) (Section 1.3). Figure 1.4 shows the global surface temperature change for a variety of emissions scenarios. Note the uncertainty both within each emissions scenario and across the scenarios. The right hand side of figure 1.4 contains partial global maps of the projections for both high and low emissions scenarios. Note the large warming in the Arctic under the high emissions scenario. The implications of a large warming in the Arctic, and the importance of the Arctic region, will be explored in Section 1.1.2.

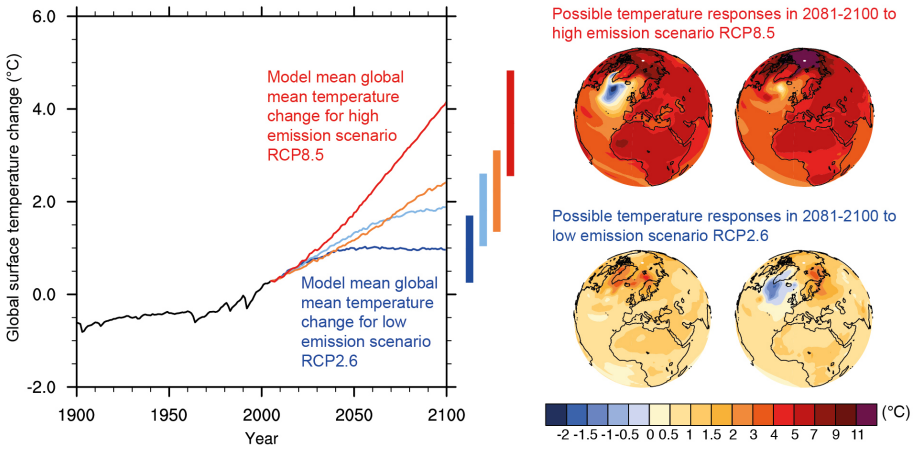

Figure 1.4: Global Mean Temperature Change Averaged Across All CMIP5 models relative to 1986-2005 for the Four RCP scenarios are displayed on the left. On the right, maps of Surface Temperature Change for the High and Low Emission Scenarios (Collins et al., 2013).

1.1.2 Arctic

The Arctic has been warming much faster than the tropics, especially in recent decades (Fig. 1.3). In recent years, the warming has increased, and the current warming has been approximately 1°C per *decade* for the past three decades (Christensen et al., 2013). This is explained largely by Arctic Amplification. Arctic Amplification results from a variety of factors present in a warming world. The primary factor is sea ice and snow cover feedback: a warming planet melts sea ice and snow cover, decreasing the albedo and allowing increased absorption of solar radiation, which in turn increases the temperature and melts more snow and ice (Hansen et al., 1997). Another major contribution to Arctic Amplification is an increase in poleward heat transport associated with a warmer planet (Alexeev et al., 2005).

Evidence for changes in sea ice are summarized in Figure 1.5. Since 1979 (the year daily satellite images of the Arctic became available), there has been a marked decrease in annual ice extent (-3.8±0.3 % per decade), multi-year ice coverage (-0.80±0.2 x 10^6km^2 per decade), and ice thickness (-0.62 m per decade) (Vaughan et al., 2013). There has also been

an increase in sea ice drift speed (almost 1 km per day per decade) and an increase in the average length of the melt season (5.7±0.9 days per decade).

The CMIP5 model projections agree that the Arctic will continue to warm faster than the tropics, though they don't agree on the magnitude of Arctic Amplification (Collins et al., 2013). For the RCP4.5 emissions scenario, the ensemble-mean winter warming is 5.0°C over pan-Arctic land areas by the end of the 21st century, while warming over the Arctic sea is 7.0°C. The increases in summer warming are more modest (2.2°C and 1.5°C respectively) (Christensen et al., 2013).

Changes in the Arctic directly affect the livelihoods of communities in the region and the various ecosystems that comprise the far north. In addition, these changes can affect people of lower latitudes through the interconnections that tie the atmosphere and the surface together.

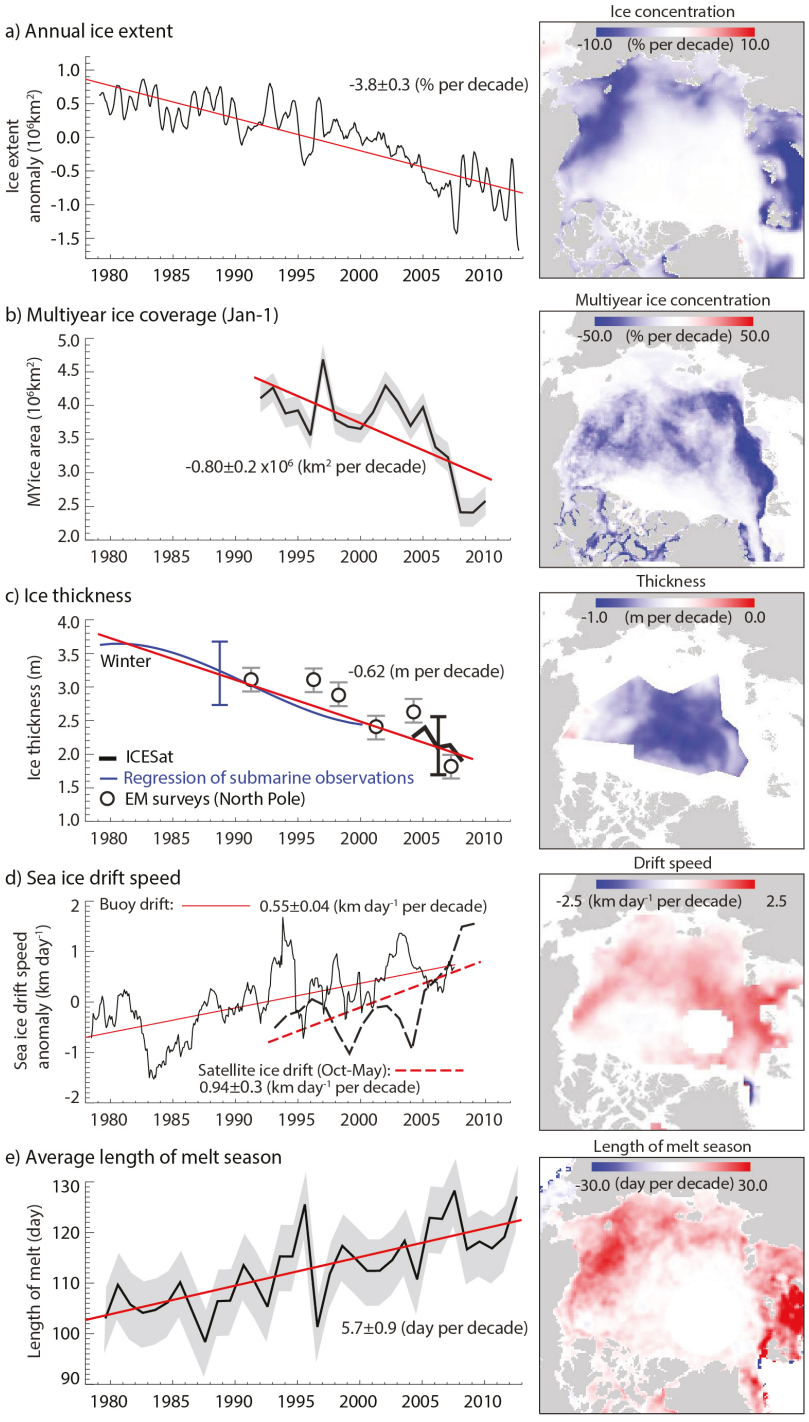

Figure 1.5: Summary of Linear Decadal Trends and Patterns of Sea Ice Extent, Multi-Year Sea Ice Coverage, Sea Ice Thickness, Sea Ice Drift Speed, and Length of Melt Season (Vaughan et al., 2013).

1.1.3 Radiative Forcing

Radiative forcing (RF) is the net change in the energy balance of the Earth system due to some imposed perturbation (Myhre et al., 2013). Calculated RF provides a basis for comparing some aspects of the potential climate response (especially global mean temperature) to different imposed agents.

The change in radiative forcing (RF) is related to a change in temperature (T) through a climate sensitivity parameter λ in the following equation:

$$\Delta T = \lambda RF$$

The climate sensitivity parameter λ can be estimated from GCM simulations, and may not be uniform for different forcing agents (Myhre et al., 2013).

The change in radiative forcing from pre-industrial times (1750) to the present are presented in Figure 1.6 (Myhre et al., 2013). The change in radiative forcing is influenced by several factors, including well-mixed greenhouse gases (Section 1.1.4) and aerosols (Section 1.1.5). The total anthropogenic forcing is roughly 2.3 W/m^2, with well-mixed greenhouse gases accounting for 2.83 W/m^2 and aerosol effects combining for -0.90 W/m^2. While the level of scientific understanding for greenhouse gases is Very High, the level of understanding for aerosol effects is Low or Very Low (Myhre et al., 2013). Because of this, the error bars for these effects are quite large, and much scientific progress must be made to reduce the uncertainties of the aerosol effects have on climate.

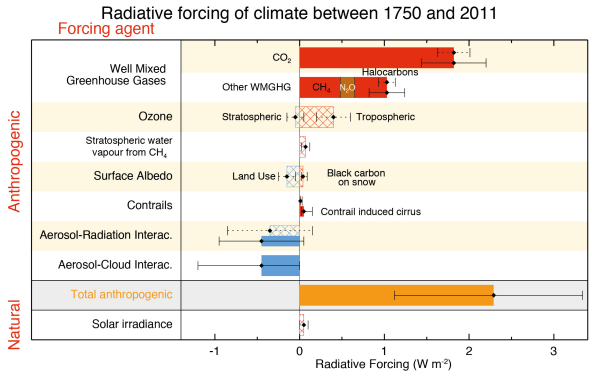

Figure 1.6: Bar Chart of Sources for changes in Radiative Forcing from the IPCC Report. Note the warming (in red) is dominated by Well-Mixed Greenhouse Gases, while the cooling (in blue) is dominated by Aerosol Effects. Also note the uncertainty bars for the Aerosol Effects (Myhre et al., 2013).

1.1.4 Greenhouse Gases

The 1750 globally averaged abundance of atmospheric carbon dioxide (CO_2) is based on measurements extracted from ice cores and ferns and is measured at 278±2 ppm (Hartmann et al., 2013). Figure 1.7 shows the CO_2 concentration since the beginning of the instrumentation record begun at Mauna Loa, Hawaii in the late 1950s. Note the long-term increase in concentration and the seasonal cycle, the latter of which is due to the larger abundance of photosynthesis and respiration in the northern hemisphere. The 2011 concentration is 390.5 ppm, with growth rates from 1980 averaging 1.7 ppm per year (Hartmann et al., 2013).

Human influences on methane (CH_4) concentrations have been present for thousands of years, resulting in a 1750 estimate of 722±25 ppb. The 2011 CH_4 concentration is 1803±2 ppb, a 2.5-fold increase over the 1750 mark (Hartmann et al., 2013). Direct atmospheric measurements of globally averaged CH_4 began in 1978 and are plotted in Figure 1.8. Note that the growth rate has slowed to a near steady-state (with strong inter-annual variability). While the prospect of increased emissions from Arctic wetlands and sub-sea clathrates is an active area of study, it is unlikely that there has yet been a permanent measurable increase

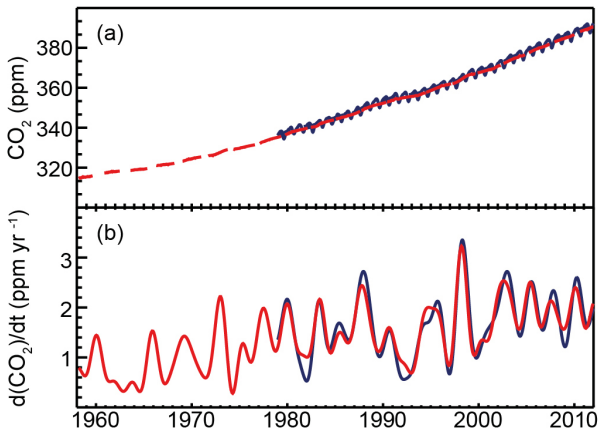

Figure 1.7: a) Globally averaged CO_2 concentrations from Mauna Loa and the South Pole in red (monthly resolution) and NOAA/ESRL/GMD in blue (weekly resolution) b) Growth Rate of CO_2 per year (Hartmann et al., 2013).

in those CH_4 emission levels.

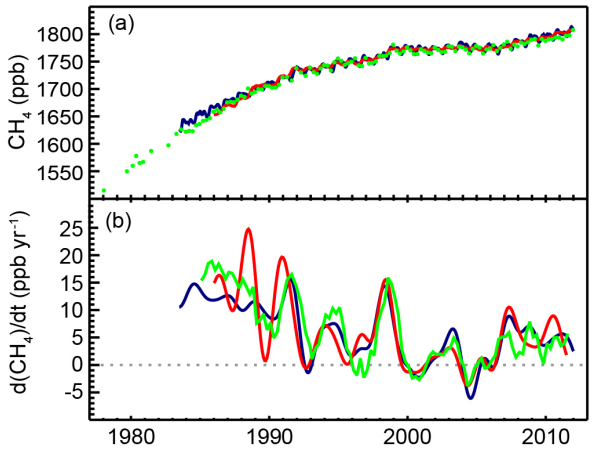

Figure 1.8: a) Globally averaged CH_4 concentrations from UCI in green (quarterly), AGAGE in red (monthly) and NOAA/ESRL/GMD in blue (weekly resolution) b) Growth Rate of CH_4 per year (Hartmann et al., 2013).

Increases in nitrous oxide (N_2O) concentration have been dominated be emissions from

synthetic and organic nitrogen fertilizers. The 2011 value of 324.2 ppb for N_2O concentration is approximately 20% greater than the 1750 estimate of 270±7 ppb (Hartmann et al., 2013). The evolution of N_2O concentration since the late 1970s is shown in Figure 1.9. Note the seasonal cycle overlaying the linear trend. It should also be noted that there are strong latitudinal gradients in N_2O concentrations, with values highest over agricultural zones such as the Northern subtropics, and lower values over the Arctic (Hartmann et al., 2013).

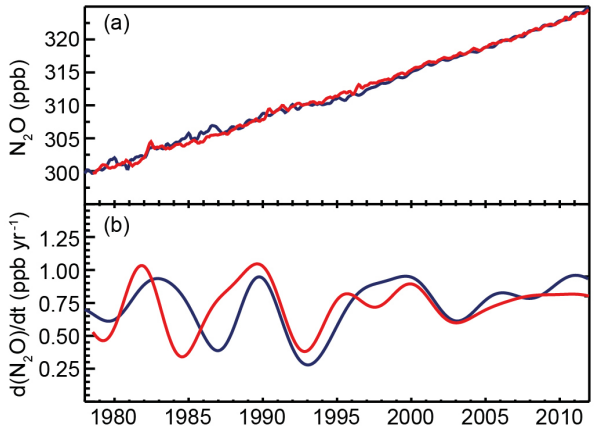

Figure 1.9: a) Globally averaged N_2O concentrations from AGAGE in red and NOAA/ESRL/GMD in blue, both at monthly resolutions b) Growth Rate of N_2O per year (Hartmann et al., 2013).

Projections of the concentrations of the well-mixed greenhouse gases are shown in Figure 1.10. Note that many of these concentrations may increase drastically under the most polluting emissions scenarios. With these increases, there is an expectation that the resulting radiative forcing of these gases will increase from their current values of 1.82±0.19 W/m^2 (CO_2), 0.48±0.05 W/m^2 (CH_4), and 0.17±0.03 W/m^2 (N_2O) (Myhre et al., 2013). This warming will more than compensate for the cooling effects of aerosols, to be discussed in Section 1.1.5. However, this does not diminish the role that aerosols play in the energy budget nor does it obviate the need for their study in that role.

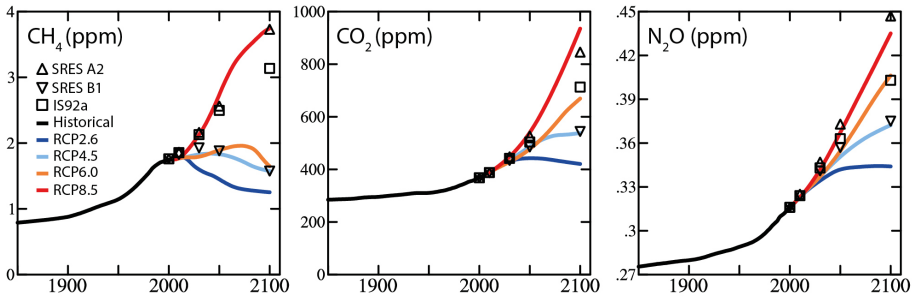

Figure 1.10: Time evolution of well-mixed greenhouse gas (CO_2,CH_4,N_2O) concentrations (black) and future projections (color) based on various RCP emissions scenarios (Myhre et al., 2013).

1.1.5 Aerosols

Aerosols are particles suspended in the atmosphere with sizes ranging from a few nanometers to tens of microns (Myhre et al., 2013). They occur as a consequence of both the natural environment (e.g., sea salt and dust) and of human activities (e.g., fossil fuel combustion and biomass burning), and can be either directly emitted as primary aerosols (black carbon, organic carbon, sea salt, dust) or may result as products of chemical reactions, or secondary aerosols (sulfate, nitrate, ammonium, secondary organic aerosols) (Myhre et al., 2013). The size and composition of aerosols can be modified by additional chemical reactions, water uptake and loss, and coagulation, which will eventually define their physical, chemical, and optical properties (Myhre et al., 2013). It is these properties that affect radiation (either directly or indirectly through clouds) and thereby influence the climate of the Earth.

There is considerable evidence that the concentration of aerosols in the troposphere has increased over the last 150 years due to human activity (Houghton et al., 2001, 306) and may increase further as developing countries grow in population and industry (Fig. 1.11). However, the effect on the surface energy balance of a further increase in aerosol loading

is extremely difficult to quantify, considering the complexity of aerosol physical, chemical and optical properties, the short time-frame in which they inhabit the atmosphere (approximately 7-10 days), and the very large heterogeneity in vertical and horizontal distribution (Boucher et al., 2013). In order to achieve a complete understanding of past and future climate change, a thorough assessment of aerosol-cloud-radiation interactions is required (Boucher et al., 2013). The current level of understanding of those interactions will be discussed in Section 1.2.

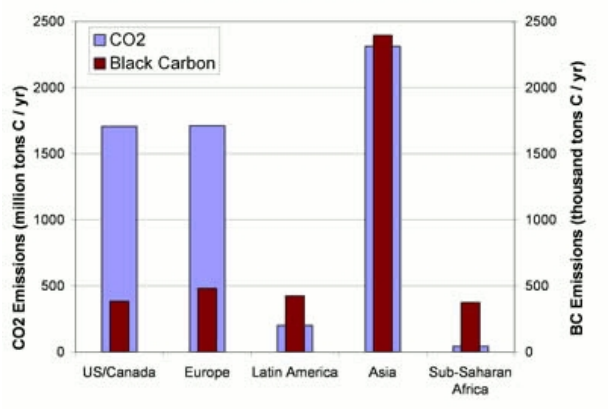

Figure 1.11: Annual Carbon Dioxide and Black Carbon Emissions by Region from (Bond et al., 2007). Note the large Black Carbon Emission from Asia: global transport will bring some of that Black Carbon to the Arctic.

1.2 Aerosol Effects

Aerosols effect the surface energy balance through a variety of forcing and feedback pathways (Boucher et al., 2013). Figure 1.12 shows the complex structure of these pathways. It can be instructive to divide the effects of forcing into three groups. The direct effect (Section 1.2.1), where aerosols interact directly with radiation, the semi-direct effect (Section 1.2.2), whereby absorbing aerosols change the atmospheric structure (with subsequent effects on radiation), and indirect effects (Section 1.2.3), wherein aerosols cause changes in cloud structure. These effects are explained in Figure 1.13.

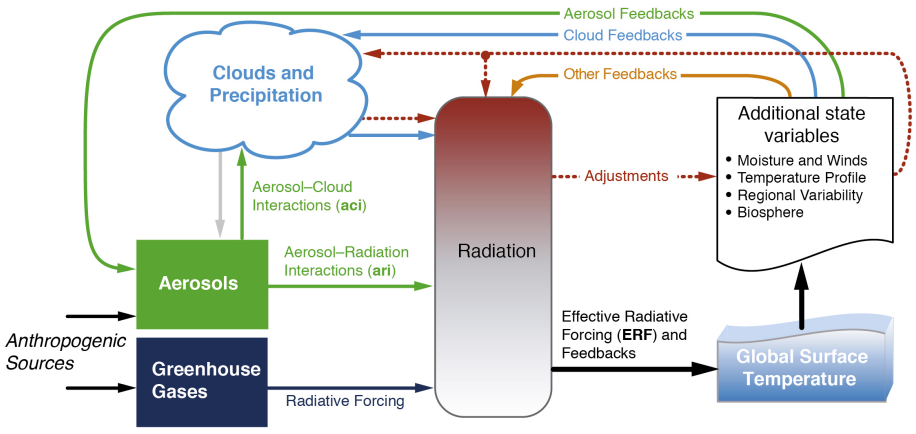

Figure 1.12: Schematic of the feedbacks, forcing, and interactions between Aerosols, Clouds, Radiation, and the Surface Temperature (Boucher et al., 2013).

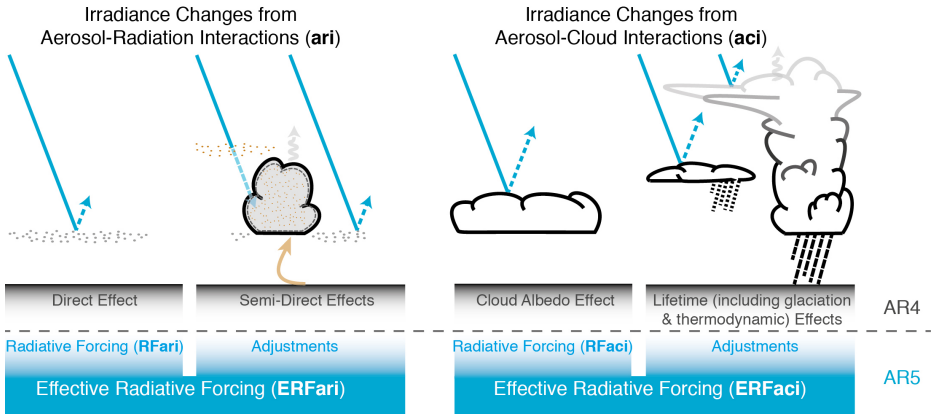

Figure 1.13: Schematic of Aerosol Direct, Semi-Direct, and Indirect Effects. Note the terminology changes used in the AR5 report (Boucher et al., 2013) with respect to the AR4 report (Solomon et al., 2007).

1.2.1 Aerosol Direct Effect

The aerosol direct effect is the effect aerosols have on radiative forcing by absorption and scattering. Atmospheric aerosols intercept incoming solar radiation and will either absorb the photon (generating local heat) or scatter the photon, depending on the species of aerosol (Boucher et al., 2013). See Figure 1.14 for an illustration. Both methods reduce the amount of solar radiation reaching the surface of the Earth. Absorbing aerosols (such as black carbon) and their interactions with solar radiation will be discussed in detail in the semi-direct effect section (1.2.2). Scattering aerosols such as sulfates block incoming solar radiation from reaching the surface and reflect it back to space through Mie scattering (Haywood and Boucher, 2000). This is because aerosols are typically in the 0.1-2 μm size range, which is the range for which Mie scattering is effective for visible light (solar radiation). This scattering represents a negative forcing to the atmospheric radiation budget. The current best estimates indicate a negative forcing from the globally averaged aerosol direct effect of -0.35$\pm$0.5 W/m^2 (Boucher et al., 2013). The main sources of uncertainty in these estimates include uncertainties in the emission levels and size distributions of aerosols, as well as uncertainties in the optical properties of sulfates that are either internally or externally

mixed with non-sulfate aerosols.

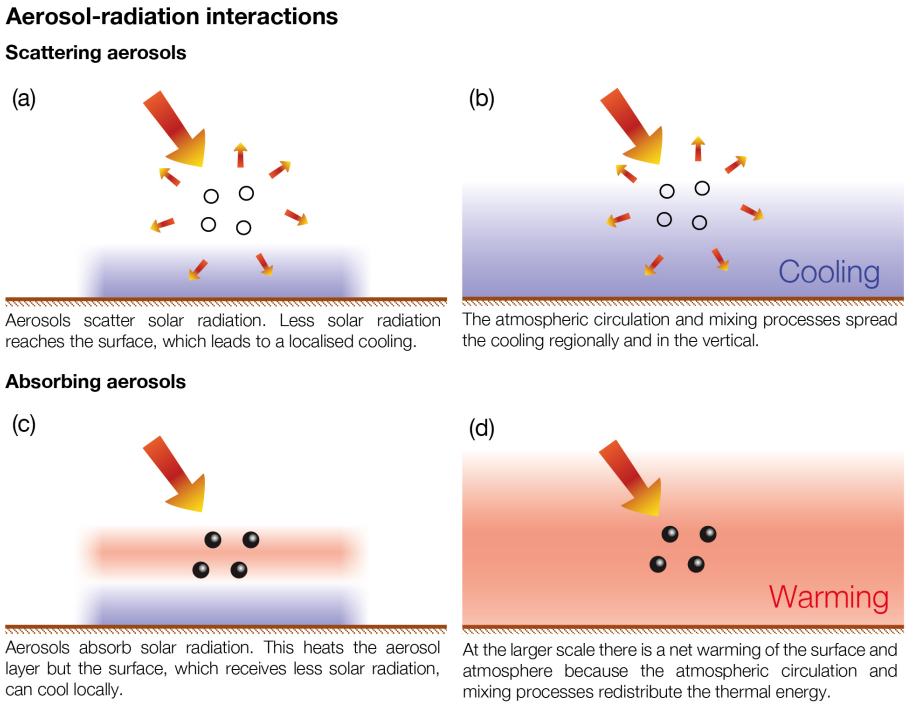

Figure 1.14: Schematic of the Aerosol Direct and Semi-Direct Effect: top) scattering, bottom) absorption (Boucher et al., 2013).

1.2.2 Aerosol Semi-Direct Effect

As mentioned in the Aerosol Direct Effect Section (1.2.1), aerosols either absorb or scatter radiation. Certain species of aerosols, such as black carbon, are highly absorbing. When these aerosols are in the atmosphere, they absorb incoming solar radiation, and re-emit the absorbed energy as heat. If this heating of the atmosphere occurs near clouds or areas of atmospheric moisture, it will reduce cloud cover in the area (Hansen et al., 1997). This reduction of cloud cover enables more solar radiation to reach the surface, thereby inducing a positive radiative forcing.

As emission levels of black carbon have increased since the pre-industrial era (Bond et al., 2007), the semi-direct effect may have a significant impact on climate forcing. However, local forcing will depend highly on the aerosol distribution and on local cloud conditions. At present, the estimate of the global semi-direct Effect is 0.2 W/m^2, though there is very low confidence in the magnitude and sign of this estimate (Boucher et al., 2013). Obtaining a global average is further complicated by the uneven geographic distribution of black carbon emissions (Fig. 1.11). In addition, the vertical position of the black carbon relative to the cloud is crucial in determining the magnitude of the effect (Lindeman et al., 2011) and this position is poorly represented by GCMs. The warming of the semi-direct effect may offset or partially offset the cooling of the direct and indirect effects, but more research, including integrated modeling and observational analysis studies, needs to be performed in this area.

1.2.3 Aerosol Indirect Effects

Aerosol indirect effects are so named because the aerosols alter the microphysical and radiative properties of clouds, which in turn will alter the radiative forcing at the surface. This is accomplished through two major indirect effects and several minor indirect effects, which operate mostly on mixed-phase clouds.

The first indirect effect, also known as the albedo effect (or Twomey effect), was described by Twomey (Twomey, 1977). This effect describes the ability of some aerosols to act as cloud condensation nuclei (CCNs). This increase in CCNs results in an increase in the number of water droplets in the cloud, but the size of the droplets is smaller. This makes a cloud brighter in appearance, and so will reflect more incoming solar radiation than a clean cloud. Thus, there is a negative radiative forcing effect from the Twomey effect. See Figure 1.15 for an illustration.

The second indirect effect, also known as the lifetime effect, is also the result of aerosols

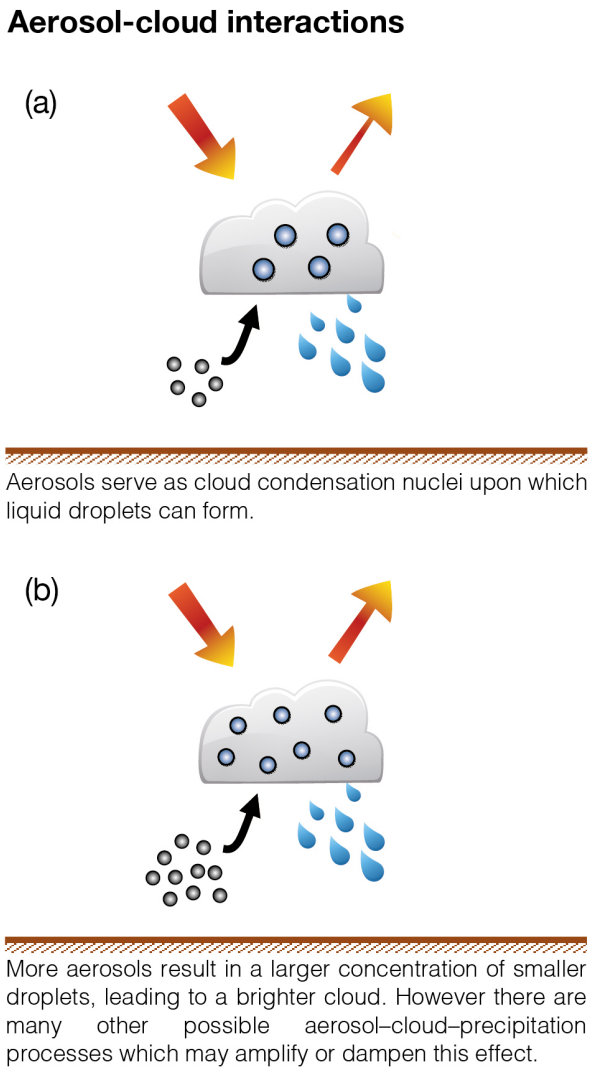

Figure 1.15: Schematic of the First Aerosol Indirect Effect: top) cloud with few aerosols, bottom) cloud with more aerosols (Boucher et al., 2013).

acting as cloud condensation nuclei. In addition to making the cloud brighter in appearance, the presence of aerosols inhibits precipitation because the cloud droplets are smaller, as the larger number of CCNs now competes against the existing moisture amount. This aerosol effect increases lifetime of clouds and is first observed by Albrecht (Albrecht, 1989). The increased lifetime of the cloud in the atmosphere results in less solar radiation hitting

the surface, and a further negative forcing.

There are further indirect effects that influence mixed-phase clouds. The presence of aerosols in optically thin liquid clouds can generate a positive surface forcing through increased longwave emissivity (Garrett and Zhao, 2006). The glaciation effect describes how aerosols can act as ice nuclei in clouds with temperatures between 0 and -38 ° C (Lohmann and Lesins, 2002). This increases the precipitation efficiency in these clouds, leading to shorter cloud lifetimes and a positive radiative forcing. However, soluble aerosols such as sulfates can hinder glaciation, depressing the freezing temperature of supercooled drops to the homogenous freezing point (Girard et al., 2005). Another indirect effect is the thermodynamic effect (Rosenfeld, 1999). The presence of aerosols in the thermodynamic effect results in smaller cloud droplet sizes, which in turn delays the onset of freezing in convective clouds. It is not clear whether this has a positive or negative effect on the radiative balance.

Mixed-phase Arctic clouds persist for extended periods on the order of days or weeks, despite the fact that an ice-water mix is inherently unstable (Boucher et al., 2013). The low ice nuclei (IN) concentrations that exist (1 in every 10^6 particles acts as an IN (Morrison et al., 2012)) enable the clouds to persist for these long periods, as a higher IN load would result in increased glaciation and dissipation of the cloud (Ovchinnikov et al., 2011). There is increasing evidence that ice forms in Arctic stratus via immersion freezing (from the liquid phase), which means CCN concentration (and by extension, aerosols) will play a role in sustaining these clouds (de Boer et al., 2011). This would represent a self-regulating feedback for sustaining the clouds: as ice formation is initiated by liquid droplets, ice grows, which depletes liquid water (through the Wegener-Bergeron-Findeisen process (Korolev, 2007)), suppressing further ice growth (Morrison et al., 2012) See pathway "c" in Figure 1.16 for a schematic.

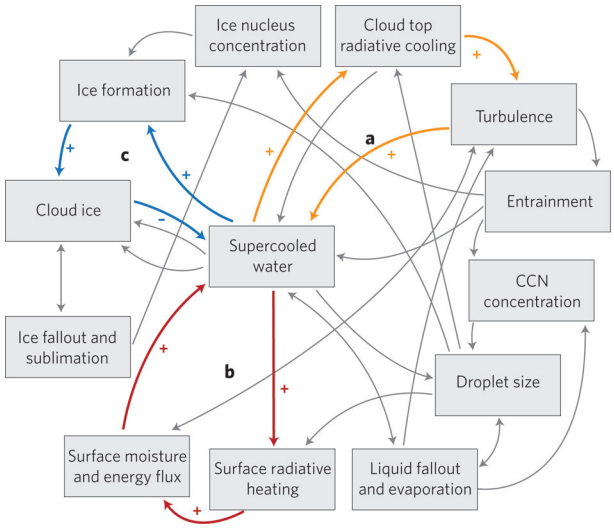

Figure 1.16: Schematic of processes associated with Arctic mixed-phase clouds (Morrison et al., 2012).

The complexity of the various aerosol indirect effects makes an estimate of forcing difficult. The GCM estimates have a median value of -1.37 W/m^2, yet sulfate is the only species considered and only the first indirect effect is considered (Boucher et al., 2013). The inevitable uncertainty in these results is due in part to the coarse resolution of GCMs, which are unable to accurately depict relevant updraft velocities which are crucial for cloud formation and aerosol activation. GCMs also have difficulty with super-cooled clouds and non-spherical ice nuclei shapes.

1.3 Models

Because the physical processes that affect our climate occur at a variety of spatial and temporal scales, it is important to investigate said processes with a variety of tools. Observations, both *in situ* and remote, as well as laboratory experiments, enhance our understanding of climate phenomena. With the advent of computerized numerical simulation, or modeling, an additional tool is now available with which we can study climate processes.

Climate models come in a variety of scales; the choice of model is dependent on the topic of study. Global models (GCMs) (Section 1.3.1) may be run for simulations for hundreds of years and encompass the entire planet. Fine-scale models, such as large eddy simulations (LESs) or cloud resolving models (CRMs) (Section 1.3.2), have runs lasting hours or days, with a horizontal extent measured in hundreds or thousands of meters. Regional models (Section 1.3.3) fall between global and fine-scale models in both temporal and spatial depth.

1.3.1 Global Models

The primary function of global models (GCMs) is to understand the dynamics of the atmosphere, ocean, land, and sea ice: the physical components of the climate system. With knowledge of those components, it is possible to make projections about future climate based on forcing agents such as greenhouse gases and aerosols (Flato et al., 2013). Models that include more advanced biogeochemical cycles are often termed Earth System Models (ESMs).

The Coupled Model Intercomparison Project Phase 5 (CMIP5) is a coordinated suite of global model simulations designed to distinguish the errors inherent to a particular model from the errors faced by the modeling community as a whole (Flato et al., 2013). The climate projections discussed in previous sections are based on results from CMIP5, and the models also help constrain present-day forcing estimates.

Note that the projections and present-day estimates are globally-averaged quantities, and for certain processes (such as aerosol-cloud interactions), the uncertainties are large. This is likely a reflection of the large gap that exists between our process-level understanding of aerosol-cloud interactions and the ability of GCMs to represent them (Boucher et al., 2013). Historically, GCMs have used simple constructs for aerosol-cloud interactions (such as the Twomey and lifetime effects). Aerosol activation and ice nucleation have seen progress in recent years in GCM parameterization schemes. However, the key physical processes in aerosol-cloud interactions occur at the fine scale and cannot be adequately represented at coarser resolutions (Boucher et al., 2013).

1.3.2 Fine-Scale Models

Fine-scale LES and CRM models have greatly advanced as a tool for testing the physical mechanisms of climate systems that operate at a small scale, such as aerosolcloud interactions. Because they can explicitly solve many of the important mechanisms of cloud development (specifically vertical velocity), they do an excellent job simulating cloud properties. Like GCMs, however, they too have limitations. The main obstacle is that they are idealized, so they do not resolve synoptic scale circulations or allow for representation of orography (Boucher et al., 2013). For liquid clouds, various aerosol impact mechanisms tend to be mediated by interactions across scales not included in the idealized albedo and lifetime effects. For example, the dependence of precipitation development in stratiform clouds depends on details of the vertical structure of the cloud. This hints that liquid clouds may not be as sensitive to aerosol loading as global models would suggest. Similar behaviour in mixed-phase stratus, which are prevalent in the Arctic, are beginning to be documented but even process-level understanding, let alone representation in models, is much less advanced (Boucher et al., 2013).

1.3.3 Regional Models

Regional models are a medium between the large-scale and the small-scale. They allow for a focus on an area of interest (such as the Arctic), enabling computational cost to be directed towards a higher resolution than global models. It also allows resources to be directed to more complex representations of physical processes (such as the aerosol life-cycle, chemistry, and cloud processes). There are still some processes which are not explicitly resolved in a regional model, but the high resolution allows parameterizations to use more information for parameter inputs.

When compared to fine-scale models, regional models include non-idealized meteorology, synoptic scale forcing, variability in land surface, and diurnal cycles (Boucher et al., 2013). This allows a more realistic interaction for certain processes (such as Arctic stratus development), which rely on synoptic scale forcing for their persistence.

1.4 Objective

The response of the climate system to the radiative forcing over the Arctic region is extremely complex due to the strong annual variation of the diurnal cycle and surface characteristics. The high surface albedo of snow and ice and unique atmospheric aerosol composition (a majority of sulfates and sea salt) make the Arctic climate system very sensitive to external forcings such as the ice-albedo feedback (Alexeev et al., 2005) and the aerosol-cloud-radiation feedback. These feedbacks have been studied extensively on many time scales (Browse et al., 2014; Girard and Blanchet, 2001; Koch et al., 2009). However, the diurnal cycle of surface temperature is also an important element of the Arctic climate system, and has not been studied extensively. There are still large uncertainties associated with the diurnal cycle of aerosol-cloud-radiation interactions and with the ability of aerosols to affect the diurnal cycle of surface temperature in the Arctic. A way to address these uncertainties is through a study using a high resolution regional climate model with an embedded atmospheric chemistry model such as WRF-CHEM, which may improve our understanding of the changes in surface temperature due to aerosol effects in the Arctic during the diurnal cycle.

Chapter 2: Methodology

The research objective of this study will be accomplished through an integrated assessment that combines analyses of observations with high-resolution simulations from the Weather, Research, and Forecasting Chemistry model (WRF-CHEM). The following paragraphs will provide a brief description of the WRF-CHEM model and the model options used, outline the model runs performed, and detail the observational data used in this study.

2.1 WRF-CHEM

WRF-CHEM (v3.1.1) is a fully compressible mesoscale meteorological model designed for operational weather forecasts as well as research experiments (Skamarock et al., 2008). The chemistry component (Grell et al., 2005) contains a variety of modules for simulating aerosol and chemistry processes. This study uses the Model for Simulating Aerosol Interactions and Chemistry (MOSAIC) aerosol scheme (Zaveri et al., 2008). This scheme allows simulation of direct, semi-direct, and indirect effects for a wide variety of aerosol species (including sulfates, nitrates, sea salt, ammonium, dust, black carbon). This is accomplished by the division of each aerosol species into up to eight size bins (Table 2.1). The aerosol microphysical properties are calculated, and aerosol, cloud, radiation, and chemistry interactions are coupled in MOSAIC.

WRF-CHEM has a discretization scheme for both spatial and temporal propagation. Horizontal and vertical advection use fifth/third-order finite differences, and the time step uses the third-order Runga-Kutta method. The WRF-CHEM model uses a microphysics scheme from (Lin et al., 1983). Other parameterization schemes include Grell cumulus,

Table 2.1: MOSAIC aerosol bin sizes

Bin Sizes		
Bin	Minimum	Maximum
1	39nm	78nm
2	78nm	156nm
3	156nm	313nm
4	313nm	625nm
5	625nm	1.25μm
6	1.25μm	2.5μm
7	2.5μm	5μm
8	5μm	10μm

Noah land surface model, Monin-Obukhov surface layer physics, Goddard shortwave radiation and Rapid Radiative Transfer Model (RRTM) longwave radiation. The chemistry package alters the Goddard shortwave and Lin microphysics schemes so that aerosol number (and by extension cloud condensation nuclei) is used in the calculations. This enables the representation of the aerosol direct, semi-direct, and indirect effects.

WRF-CHEM initial and boundary conditions are provided by the National Centers for Environmental Prediction (NCEP) Final Operational Global Analysis (FNL), which contains 1 degree horizontal resolution, 26 pressure levels, and has a 6 hour update cycle. This analysis is conformed to the WRF-CHEM grid using the WRF Pre-processing Suite (WPS). First, static geographic data is interpolated to the model grid using the program "geogrid". Then, the FNL analysis is written to an intermediate format using the "ungrib" program. Finally, the intermediate file is vertically integrated using a linear interpolation scheme, and is horizontally interpolated to the model grid using the program "metgrid". The result is a suite of 6-hourly meteorological files on the WRF domain. The program "real" from the WRF suite creates initial and boundary conditions from these files. For WRF-CHEM, gas species and aerosols must also have initial and boundary conditions. These are initialized with the Mozart-4 Reanalysis, which has a 6 hour update cycle and a 2.5 degree horizontal resolution. The program "mozbc" maps these species to variables used by the WRF-CHEM model using an editable list that is unique to each combination of aerosol and chemistry

module.

2.2 Model Runs

In order to achieve the objective of this study, several model runs are performed. A summary of the model runs is shown in Table 2.2. The horizontal extent of the simulation domain is shown in Figure 2.1, along with the terrain height. The domain is a polar stereographic grid, with a horizontal grid resolution of 10 km and a horizontal spatial domain of 3000 km by 3000 km. The 45 vertical levels have a high resolution near the surface (25 m), which gets gradually coarser towards the model top at 200 mb. This vertical spacing emphasizes the boundary layer processes that affect the surface temperature in the Arctic. The principal run is known as the Control Run. It begins at April 15th, 00Z and ends at April 21st, 00Z for a total run of 6 days. The first 3 days are considered chemistry model spinup, with the analysis period beginning on April 18th, 00Z. The Control Run utilizes the full capability of the WRF-CHEM model, with simulation of the full aerosol life cycle and aerosol number affecting the radiation and microphysics codes. This in turn allows the simulation of the total aerosol effect, including the direct, semi-direct, and indirect effects. The second run of interest is the NoChem run, which has the same start date and end date, and the same parameterizations as the Control Run. The difference is found in the treatment of aerosols in NoChem: specifically, that aerosols are prescribed at a low constant value, with no variation over time. In addition, aerosol properties are not propagated to the radiation or microphysics code, so aerosols act as a passive tracer without temporal variability. This difference in treatment allows a comparison between the runs to yield the effects of aerosols on the surface temperature.

To account for meteorological variability, a series of 6 ensemble runs is performed. Each run is identical to the Control Run aside from the start date. The start date for the ensemble Runs are: April 14th 00Z, 06Z, 12Z, and 18Z, and April 15th 06Z and 12Z. The ensemble

Table 2.2: A summary of the various model runs executed.

Name of Run	**Run Properties**
Control Run	Baseline Run with Full Suite of Chemistry Options
NoChem	Chemistry Option Turned Off, No Aerosol Effects
Ensemble 1-6	Baseline Runs starting at April 14 (00Z, 06Z, 12Z, 18Z), 2008 and April 15 (06Z, 12Z), 2008
NoAerRad	No Direct Aerosol Impact on Radiation
NoAerRadorBC	No Direct or Semi-Direct Aerosol Impact on Radiation
BC0	Black Carbon Eliminated from Emissions, Initial and Boundary Conditions

runs, together with the Control Run, compose the ensemble suite. With this suite of runs, a statistical analysis (based upon the t-test) is performed (details are discussed in Section 3) to test the significance of the difference between the Control Run and the NoChem run relative to the null hypothesis that the differences are due to meteorological variability. Finally, in order to separate the constituent aerosol effects, a series of runs are also performed that change certain interactions between aerosols and radiation and microphysics. The NoAerRad run does not have a direct link between aerosols and the radiation code, but still has black carbon and the link between aerosols and microphysics. The NoAerRadorBC run is identical to the NoAerRad run but has had black carbon removed. The difference between NoAerRad and the Control Run should yield the direct effect, as the elimination of the direct effect is the only change between the two runs. As the NoAerRadorBC run contains only the indirect effects, a difference between it and the NoChem run should yield the indirect effects. Finally, for the semi-direct effect, the Control Run is changed to eliminate black carbon and is titled the BC0 run. The difference between these two runs should yield the semi-direct effect.

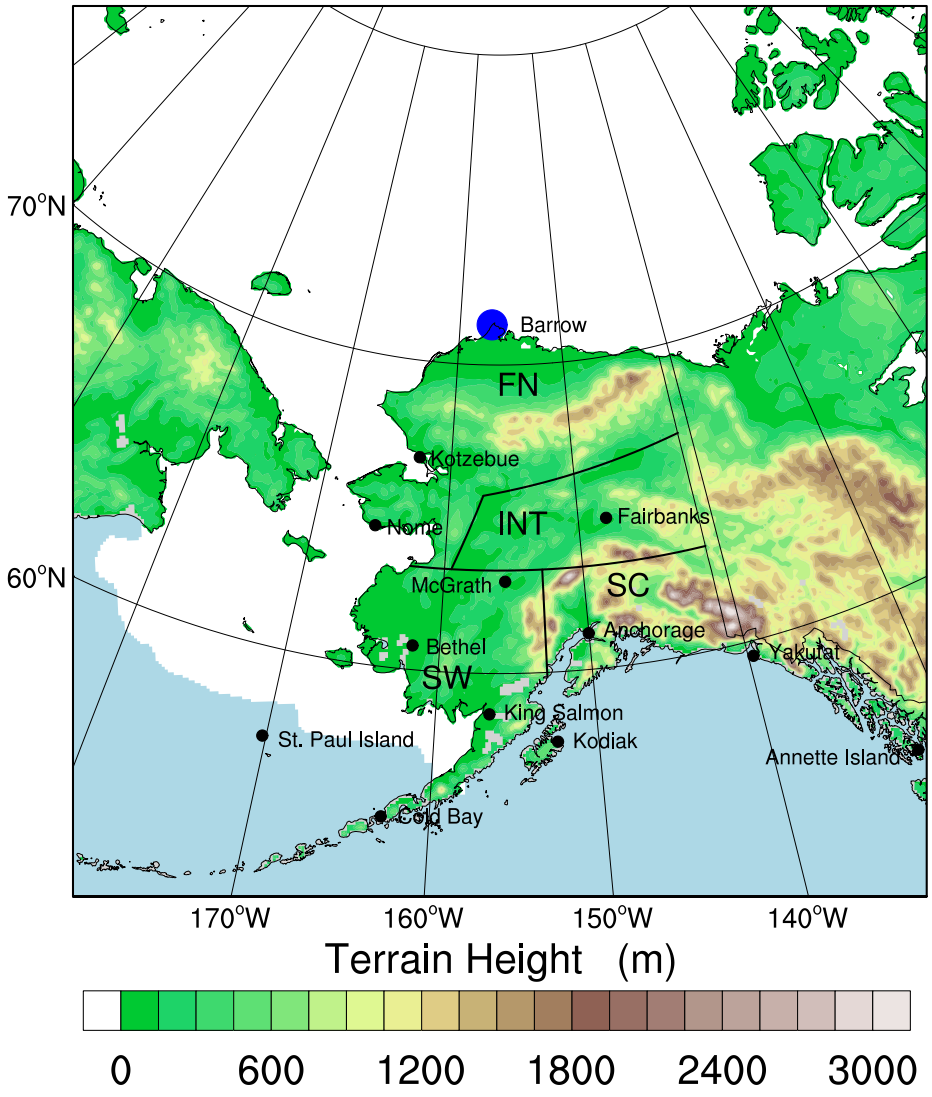

Figure 2.1: Horizontal extent of WRF-CHEM simulation domain along with the terrain height. Also shown, location of sea ice (white), open ocean (light blue), Alaska region boundaries (FN/Far North, INT/Interior, SW/Southwest, SC/South Central), radiosonde and surface observation stations, co-located at 13 airports (black dots), and the DOE NSA site at Barrow (large blue dot).

2.3 Procedure

The model performance (specifically the Control Run) is then evaluated using available observations. The Department of Energy (DOE) maintains a site in Barrow, Alaska called the

North Slope of Alaska site (NSA). The site maintains a suite of observational instrumentation used for collecting meteorological variables, with the goal of maintaining a consistent record of observations for this remote region. The Atmospheric Radiation and Measurement (ARM) program of the DOE maintains both the site and the data collection. It is from the ARM data website from which observations at Barrow are sourced. Despite the utility of the NSA site, certain properties were not able to be observed by site instrumentation alone. The Indirect and Semi-Direct Aerosol Campaign (ISDAC) was proposed for the collection of aerosol related data during the spring, to investigate the impacts of aerosols during that season. The campaign was a complement to the Mixed-Phase Arctic Cloud Experiment (MPACE) campaign that took place in the Fall of 2004 which studied similar properties under different surface conditions (mainly, no sea ice near Barrow). The ISDAC campaign took place during April of 2008 over and nearby Barrow at the North Slope of Alaska (NSA) site (cf. Fig. 2.1). The primary reason to utilize the ISDAC data is that it allows the evaluation of the Control Run, e.g., aerosol concentration. The ISDAC campaign took place during the Arctic spring, which allows a study of a stronger diurnal cycle than during other seasons. The campaign also took place during a time where several cloud types were represented, including mixed phase and glaciated clouds. Detailed information on ISDAC can be found on the DOE's ARM web site. In addition, the National Weather Service (NWS) maintains consistent sounding measurements and surface measurements at 13 airport stations throughout Alaska (cf. Fig. 2.1) with releases every six hours. These 13 stations provide meteorological observations for temperature, dew point temperature, wind speed, and wind direction against which the model is evaluated.

Chapter 3: Results

This section will first evaluate model performance against observations, then will analyze the total aerosol effect on surface energy balance components and surface temperature, and finally will attempt to separate the impact of aerosol effects on surface temperature.

A brief discussion of the synoptic background for the analysis period (April 18th, 2008 through April 21st, 2008) shows that the period begins with high pressure cells to the north and south of Alaska, both of which move off to the east over time and are supplanted by low pressure systems on April 19th and 20th. A third area of low pressure south of Russia combines with the area to the north of Alaska to form an air mass through the Bering Strait in which there is a high concentration of aerosols (discussed further in Section 3.2). Land is almost exclusively covered by snow, with depths ranging from a few cm in the south to over a meter in the mountainous areas. Sea ice covers all ocean points north of the Bering Strait and extends into the northern portion of the Bering Sea, while the southern portion of the Bering Sea and the Gulf of Alaska are ice-free (c.f. 2.1).

3.1 Model Evaluation

The goal of this section is to show that the model is performing within reasonable bounds in approximating the natural state of the atmosphere during the simulation time period. There will be two types of comparisons, point comparisons between the model and observations at Barrow, Alaska, and domain-level comparisons, through a network of radiosonde (RAOBS) and surface observations, co-located at 13 airports throughout Alaska representing a variety of terrain situations (cf. Fig. 2.1).

3.1.1 Barrow

Observed aerosol optical properties at Barrow are compared to output from the Control Run. Figure 3.1 shows both the aerosol optical depth (AOD) and the single scattering albedo (SSA) at Barrow, with the observed instrument data in blue and the model output in red. The model does not simulate AOD very well, particularly during high aerosol loading events. The model underestimates the AOD value, maintaining a relatively constant, small AOD. This may suggest the presence of a maximum aerosol optical depth limit imposed by the model (Fast et al., 2009). The SSA is a measure of absorptivity of the aerosols in the atmosphere, which ranges from 0 to 1. Aerosols with no absorptivity would measure a 1, while absorptive aerosols bring that number closer to 0. The model seems to both overestimate and underestimate the SSA during the simulation time period, suggesting that the relative value of black carbon in the model when compared to other aerosols shows less variation than in the observations, perhaps due to errors in aerosol number concentration. This representation of black carbon has been observed in WRF-CHEM before (Fast et al., 2009).

The utility of the ISDAC campaign was to collect observations of aerosols in the Arctic Spring. To do so, several flights were performed throughout the month of April, 2008. Flight 23 took off from Barrow at 8:15pm on April 18th, and flew for over 4 hours. The flight path is shown in Figure 3.2, with the red circle representing the take-off and landing point in Barrow. The result of this flight gives us the closest thing we have to an observation of aerosol number concentration for Barrow. The aerosol number concentration is crucial for model determination of aerosol indirect effects. Figure 3.2 also shows the aerosol number concentration, with the flight data taken over a 10 minute average displayed in blue, while the Control Run output, also averaged over 10 minute intervals, is shown in red. It is apparent that the model does a reasonable job in predicting aerosol number concentration, though at most times the model over-predicts the aerosol number concentration within a factor of two of observations. This might be partly due to predicted meteorological inputs

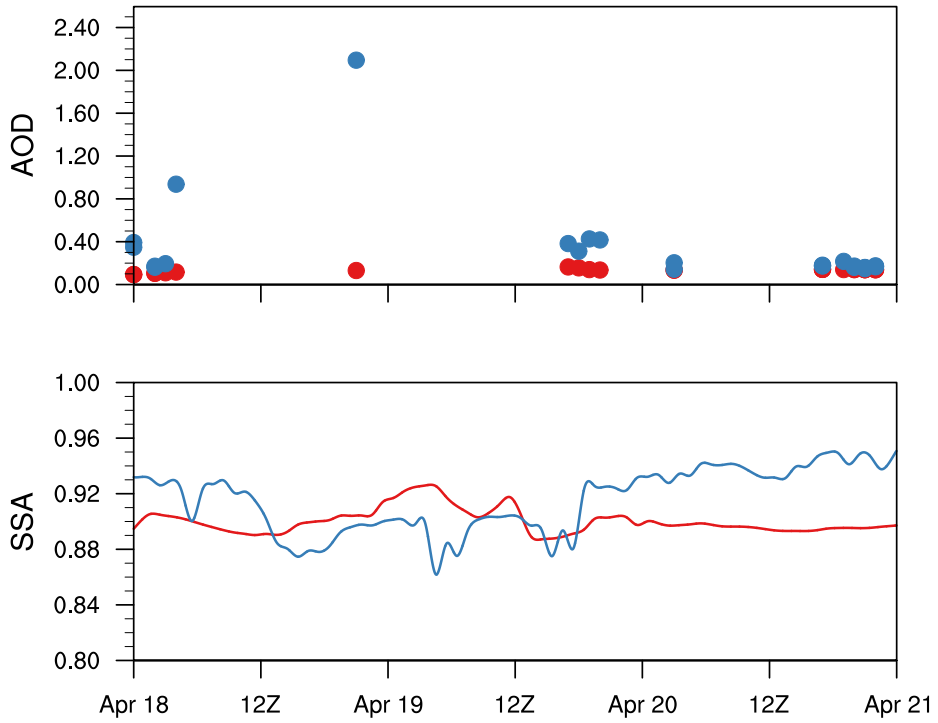

Figure 3.1: Aerosol optical depth (AOD) (markers, top panel) and single scattering albedo (SSA) (lines, bottom panel) from April 18th to April 21st, 2008 at Barrow, observations (blue) and Control Run output (red).

from the WRF model that could easily degrade the chemistry model performance (Chang et al., 2005). However, this performance satisfies air quality model acceptance criteria (i.e., concentration prediction within a factor of two of observations) as suggested by (Chang and Hanna, 2004), based on the results for many models and field experiments.

Figure 3.3 shows the model and instrument output for various irradiances and surface temperature at Barrow, with observations shown in blue and the Control Run output in red. The downward shortwave irradiance is shown in the top panel of the figure. Downwelling shortwave radiation is the principle source of energy for heating up the surface temperature during daylight hours, so it must be modeled reasonably. The Control Run tends to slightly overpredict the irradiance recorded by the instrument at the NSA site. The Control Run does a reasonable job predicting the downwelling longwave irradiance (second

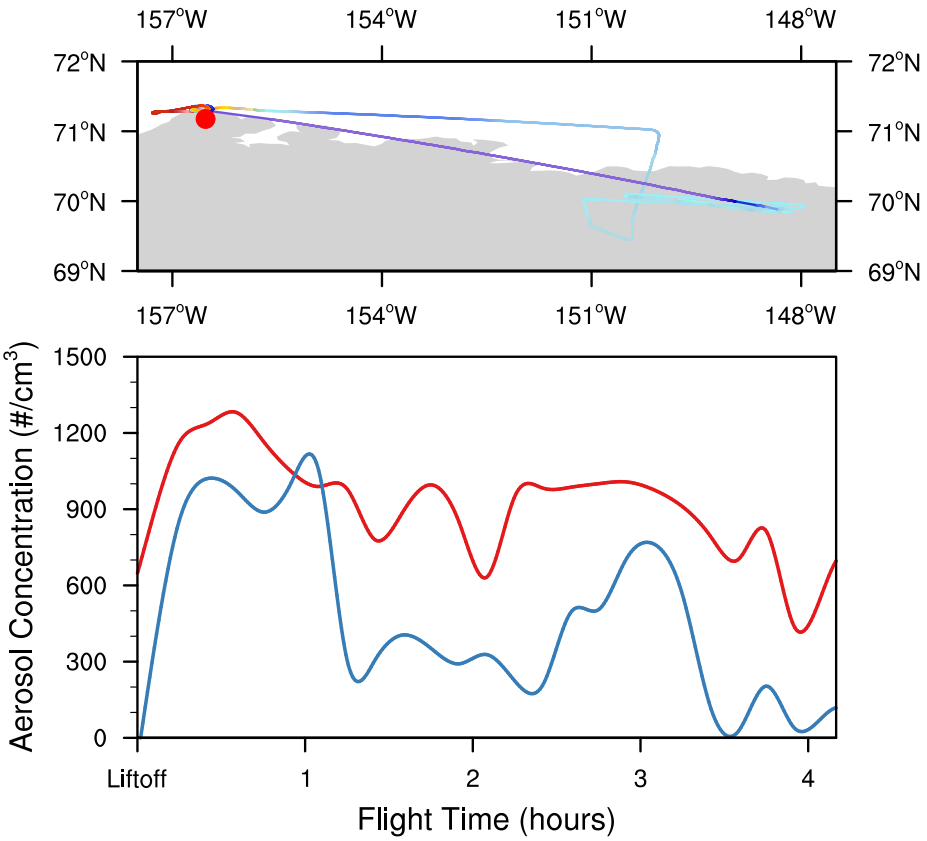

Figure 3.2: ISDAC Flight 23 path (top panel) which departed at 8:15pm on April 18th, 2008 and aerosol number concentration (bottom panel) for that flight. In the top panel, the multi-colored curve (red and orange - low altitude, cyan - middle altitude, dark blue and purple - high altitude) shows the horizontal flight path from Barrow (red circle). For the bottom panel, the Control Run aerosol number concentration (red) and flight data (blue) are averaged over 10 minute intervals.

panel of the figure), with a slight underprediction, though the temporal discrepancies tend to average out over time. It is important that downwelling longwave radiation be within appropriate bounds, as it is the driving heat source for the surface temperature at night. The upwelling longwave irradiance (third panel of Fig. 3.3) output also does a reasonable job of approximating the observations, though it, like the downwelling longwave, tends to under-predict observations. The upwelling longwave radiation is the primary driver of cooling of the surface temperature. When taken in sum, the net longwave irradiance (fourth panel of the figure) shows that the Control Run does a respectable job of matching up

with observations, with differences tending to smooth out over the simulation period. The resulting net irradiance (shortwave and longwave) from the Control Run shows good agreement with the observations at Barrow. The bottom panel of Figure 3.3 shows the surface temperature, where results show the model under-predicting low temperatures and slightly over-predicting higher temperatures. On balance, however, the Control Run does a reasonable job approximating the observed surface temperature at Barrow.

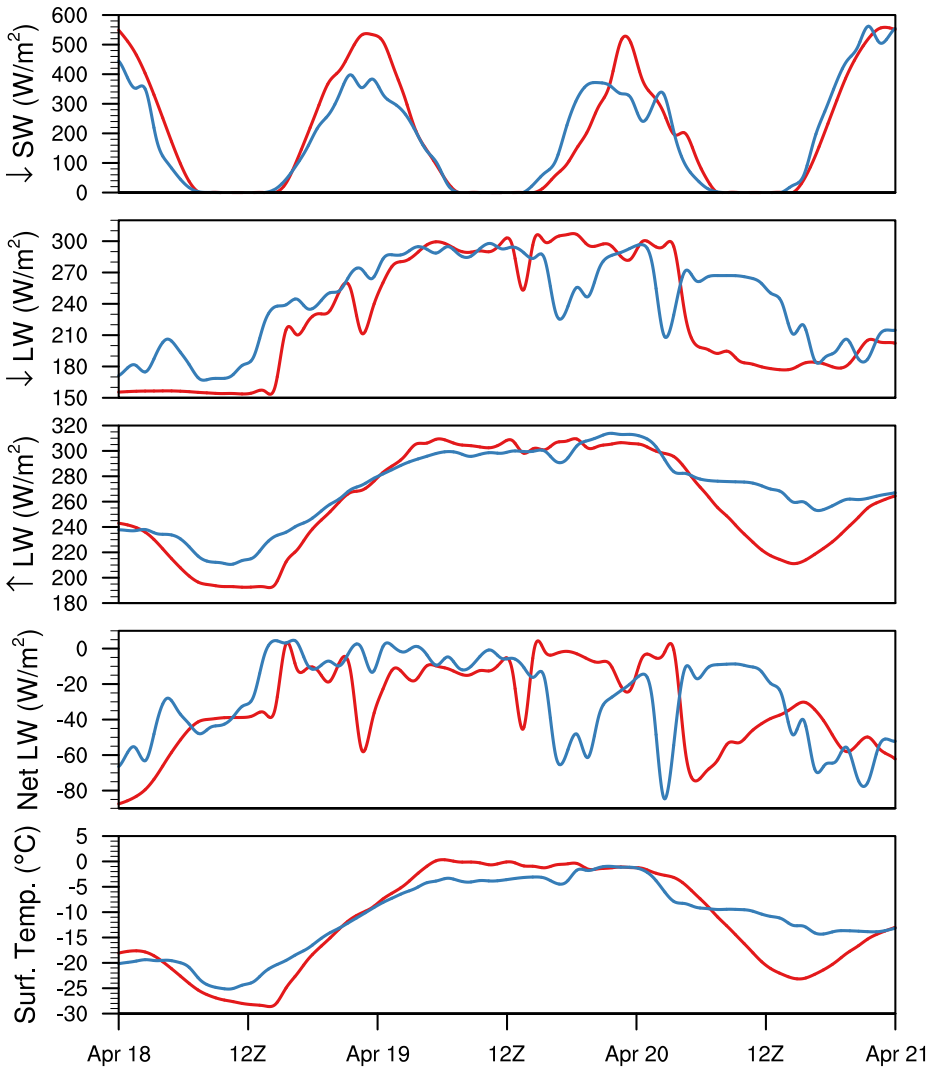

Figure 3.3: Downward shortwave radiation (top), downward longwave radiation (second), upward longwave radiation (third), net longwave radiation (fourth), and surface temperature (bottom) comparisons at Barrow from April 18th to April 21st, 2008. Control Run hourly output (red) and hourly averaged observations at Barrow (blue).

3.1.2 Model Domain

With the point comparison of the Control Run output against available observations at Barrow complete, attention is now turned to evaluation for the entire simulation domain. This will be accomplished through a series of scatter plots showing Control Run output against co-located RAOBS and surface observations from 13 airport sites in Alaska. The scatter plots and accompanying statistics show that the model is performing well within acceptable bounds from the mesoscale meteorological community for temperature, dew point, wind speed and wind direction (e. g. Boybeyi et al., 2000; Hanna and Yang, 2001; Lindeman et al., 2011). For example, an error of up to 2 °C for temperature is considered acceptable.

Figure 3.4 shows the comparisons between the RAOBS and surface observations of temperature, dew point temperature, wind speed, and wind direction at the airport stations against the Control Run model output of the same properties at those points. In addition, the surface and RAOBS statistics (mean error (ME), mean absolute error (MAE), and root mean square errors (RMSE)) are shown below the scatter plots for the respective variables at various levels. The temperature plot shows that the majority of the model output is within two degrees of the observations, which is a reasonable agreement. The surface temperature doesn't show much model bias (mean error of 0.07 °C), although the mean absolute error of 1.67 °C suggests that there is variability within these areas. However, the other three model levels (850 mb, 500 mb, and 300 mb), show very slight warm biases. Still, this is a reasonable agreement. In the dew point temperature plot, there is less agreement between the model and observations as there was for temperature. There appears to be a warm bias (2.45 °C) in the model for the atmospheric surface, which would suggest that the model has more moisture in the lowest level of the atmosphere. A slight warm (moist) bias exists for the upper model levels, which when coupled with the slight warm bias in the temperature, suggests that the average upper level model humidity accords well with observations, though there is variability between results. The wind speed plot shows that the model matches the observed wind speed reasonably well up to the 300 mb level.

However, at the 300 mb level, Control Run output shows a large mean absolute error as compared with RAOBS (this error is about 15% of the average wind speed magnitude at 300 mb). This error might be due to inaccuracies in the reanalysis fields at that height over the Arctic. At the surface, there is also a slight under-prediction bias (-0.18 m s^{-1}) for the wind speed. This may have a slight impact on properties like latent and sensible heat fluxes at the surface, which may in turn affect how the surface temperature responds. As for the wind direction, it becomes more accurate with an increase in altitude, as expected, which is important for the advection of appropriate synoptic scale systems over the region.

The model performance has shown that the Control Run overall performs reasonably well when compared to the observations available. Clearly, some errors and biases exist, but they are well within acceptable bounds when compared to other regional scale model performances. With the model performance evaluated, it is prudent to proceed with the the study of the effects of Arctic aerosols on the surface temperature using WRF-CHEM. The resulting differences between WRF-CHEM model runs are used to determine these aerosol effects, and are discussed in subsequent sections.

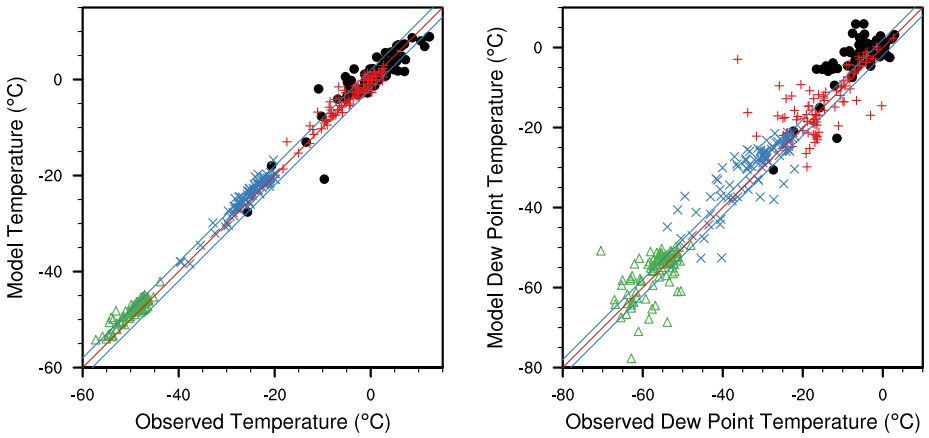

	NP	ME	MAE	RMSE
Surface	91	0.07	1.67	2.48
850 mb	90	0.40	1.19	1.59
500 mb	91	1.10	1.27	1.54
300 mb	74	1.58	1.67	2.56

	NP	ME	MAE	RMSE
Surface	91	2.45	3.23	4.54
850 mb	90	1.02	4.21	6.41
500 mb	91	1.77	3.54	4.73
300 mb	74	0.48	3.44	4.86

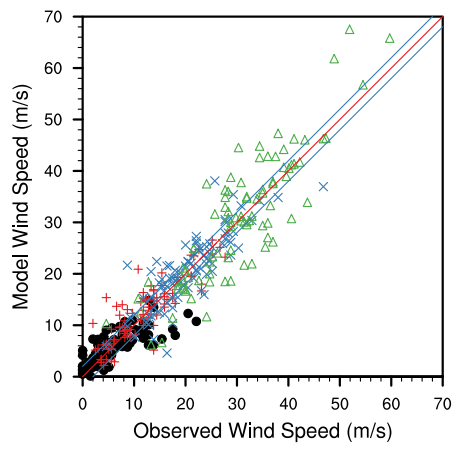

	NP	ME	MAE	RMSE
Surface	91	-0.18	2.17	3.13
850 mb	90	0.75	2.33	3.18
500 mb	91	0.03	2.89	3.94
300 mb	74	0.18	4.81	6.18

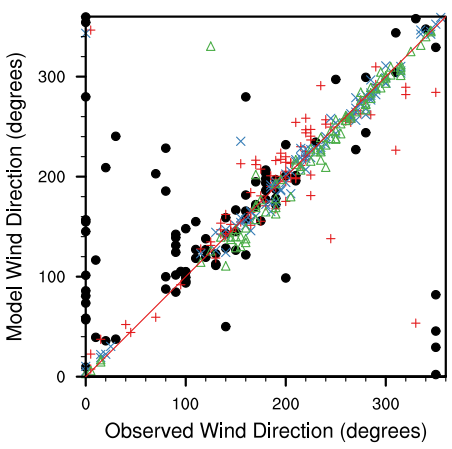

	NP	ME	MAE	RMSE
Surface	91	21.60	60.21	106.60
850 mb	90	3.09	23.25	52.50
500 mb	91	2.82	10.99	37.82
300 mb	74	-2.76	10.14	24.74

Figure 3.4: Scatter plots of temperature (top left), dew point temperature (top right), wind speed (bottom left), and wind direction (bottom right), Control Run vs observations, for 4 vertical levels: surface (black dot), 850 mb (red cross), 500 mb (blue x), and 300mb (green triangle). The red line indicates agreement between the model and the observation while the blue lines indicate agreement within 2 °C (temperature, dew point temperature) or 2 m s^{-1} (wind speed). Below each plot, the table of statistics shows the number of points (NP), the mean error (ME), the mean absolute error (MAE), and the root mean square error (RMSE) at each level.

3.2 Total Aerosol Effects

Section 3.2 will focus on the series of model runs performed to achieve the stated objective, which is to investigate aerosol effects on the Arctic surface temperature during the diurnal cycle. Aerosols affect the surface temperature through changes in cloud properties, radiative fluxes, and other surface energy balance components. This section will explore how these components change as a result of the total aerosol effect. For each component, the changes between the Control Run and the NoChem run are examined. The result will be the changes due to the total aerosol effect plus the changes due to meteorological variability. With the aid of the ensemble runs, the differences between the Control Run and the NoChem run will be masked such that the resulting differences can be attributed to the total aerosol effect.

The significance of a difference between forecasts will be tested using a variant of the t-test (Wilks, 1995), which has been employed in many scientific and atmospheric applications (e. g. Anderson and Stern, 1995; Hamill, 1999). This variant is needed because ensemble information is available only for the Control Run. We assume that uncertainties due to initial condition errors have the same statistical properties regardless of aerosol physics. Accordingly, the variance $\hat{\sigma}^2$ due to initial condition errors can be estimated from the Control Run alone as

$$\hat{\sigma}^2 = \frac{1}{E-1}\sum_{e=1}^{E}(C_e - \bar{C})^2, \tag{3.1}$$

where C_e is the value of a single ensemble member, $\bar{C}$ is the ensemble mean, and E is the ensemble size for the Control Run forecast from the ensemble suite. Under the null hypothesis that the change in aerosol physics has no impact on the forecast, the difference between the ensemble mean control forecast and NoChem forecast should have $1 + 1/E$

times the variance $\hat{\sigma}^2$. Thus, a t-statistic for testing this null hypothesis is

$$T = \frac{\bar{C} - w}{\hat{\sigma}\sqrt{1 + \frac{1}{E}}}, \tag{3.2}$$

where T is the t-statistic, w is the NoChem forecast, and $\hat{\sigma}$ is the sample standard deviation. Note that in this study the ensemble suite consists of seven members due to the computational and storage requirements of WRF-CHEM runs. However, this should not limit the study, as the t-test can provide value even with ensemble sizes as small as five (de Winter, 2013).

To reject the null hypothesis, the calculated t-statistic must be greater than the corresponding T value for the appropriate degrees of freedom and confidence interval. For the two-tail confidence interval of 0.05 and the six degrees of freedom for this ensemble, the corresponding T value is 2.447. The absolute value of the t-statistic must be greater than 2.447 in order to reject the null hypothesis with 95% confidence. The significance mask calculates the T statistic at each horizontal grid point for each component at the specified time. If the t-statistic does not exceed the aforementioned T value of 2.447, then the data is considered noise (i.e., could be a combination of aerosol effect and/or meteorological variability) and is masked. The differences that have not been masked are indicative of the changes wrought by the total aerosol effect.

The figures below will take a specific form. Each four panel plot will show output at the following times in the year 2008: the upper left panel will show April 19th, 12Z (local 1:30am), the upper right panel will show April 19th, 18Z (local 7:30am), the lower left panel will show April 20th, 00Z (local 1:30pm), and the lower right panel will show April 20th, 06Z (local 7:30pm). These times were chosen for brevity as a representative of the diurnal cycle during the 3 day analysis period (note that other diurnal cycles in the analysis period

show similar results).

3.2.1 Aerosol Number

The key component that drives the total aerosol effect is, unsurprisingly, the aerosols. Knowing the location of the aerosols will help determine their effects on other key components, and in turn their effect on the surface temperature. The first two plots (Figs. 3.5 and Fig. 3.6) show the column-averaged aerosol number concentrations from the Control Run. Figure 3.5 shows the "fine" aerosol particles that are less than 1.25 μm in radius (Kogan et al., 2011) (i.e., bins 1-5), while Figure 3.6 shows the "coarse" aerosol particles which are greater than 1.25 μm in radius (i.e., bins 6-8). Areas of high concentration for total fine aerosols include the southwestern part of the domain up along the Russian coast and crossing over Alaska near Barrow. A second plume is located in the southwest portion of the state and extends southward over the ocean and out of the domain. The coarse aerosols tend to be confined to the lower portion of the domain over Southwest Alaska. The extent of water vapor is shown in Figure 3.7. In the areas where water vapor and aerosols intersect, we should expect to find aerosols functioning as cloud condensation nuclei (CCN). The next two figures (Figs. 3.8 and 3.9) show the locations of those aerosols. The figures are similarly partitioned by size into "fine" and "coarse" modes (Kogan et al., 2011). Determining CCN concentrations and their spatial and temporal variations are key challenges in quantifying aerosol indirect effects. There are several notable locations of high concentration for fine particle CCN, including the Aleutian islands and the area to their north, off the southern coast of Alaska in the eastern portion of the Gulf of Alaska, along with locations within the Bering Strait. Coarse particle CCN locations are a subset of the fine particle CCN locations, mostly confined to the lower portion of the domain near the Aleutian islands and Southwest Alaska. Note that the coarse aerosol concentration is two orders of magnitude lower than the fine aerosol concentration. These results depict that CCN is determined by the aerosol size distribution, so that fine aerosols serve as CCN.

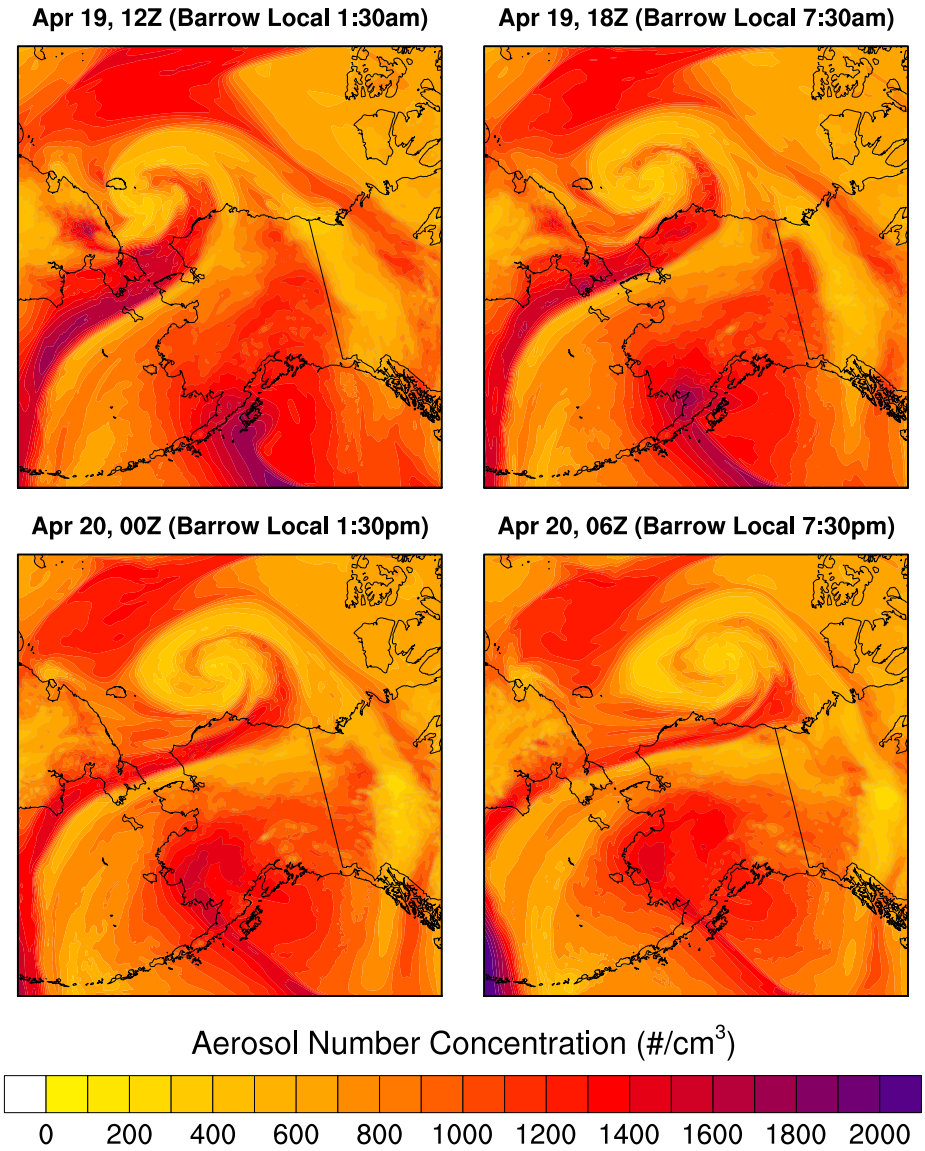

Figure 3.5: Column-averaged fine aerosol number concentration (Bins 1-5) from the Control Run for the study domain at four different times during the diurnal cycle of April 19-20, 2008.

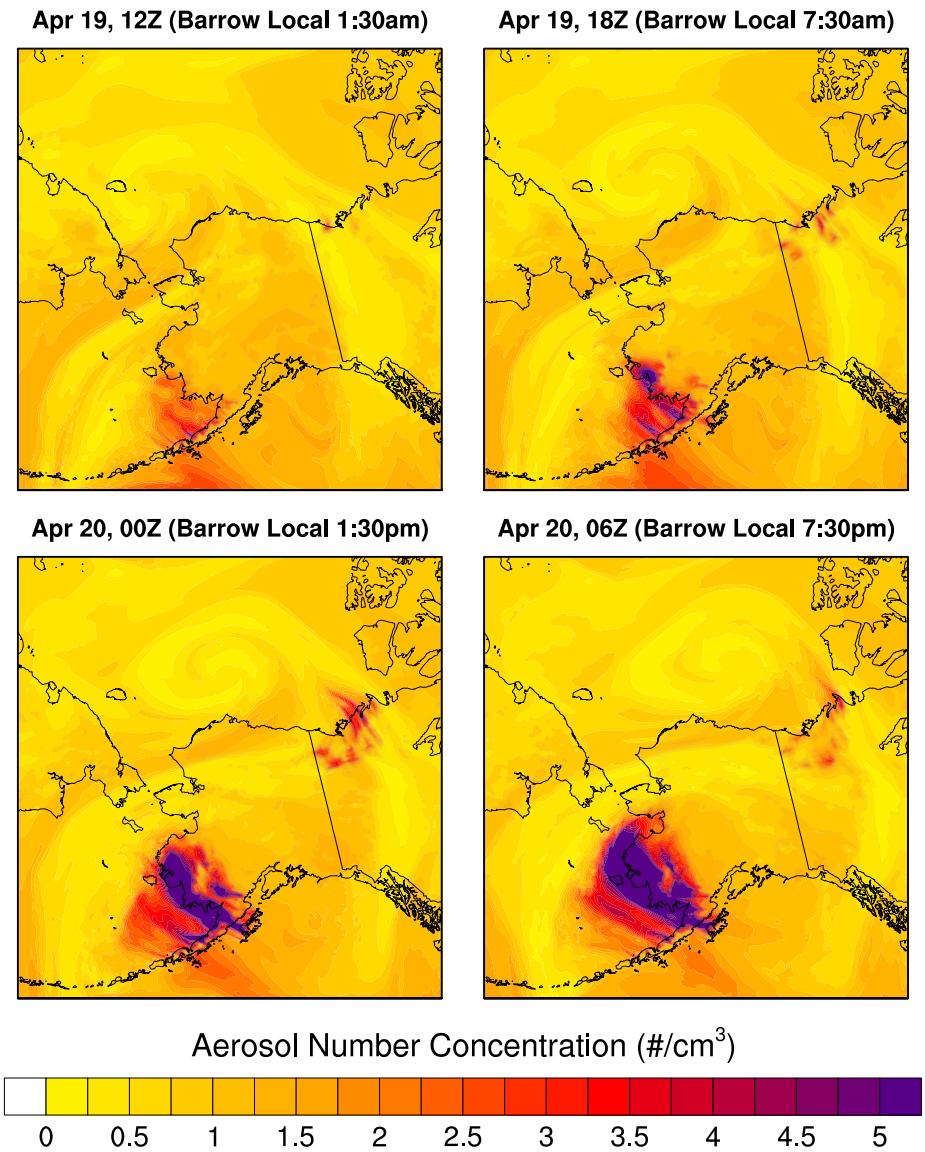

Figure 3.6: Same as Figure 3.5, except for coarse aerosol number concentration (Bins 6-8).

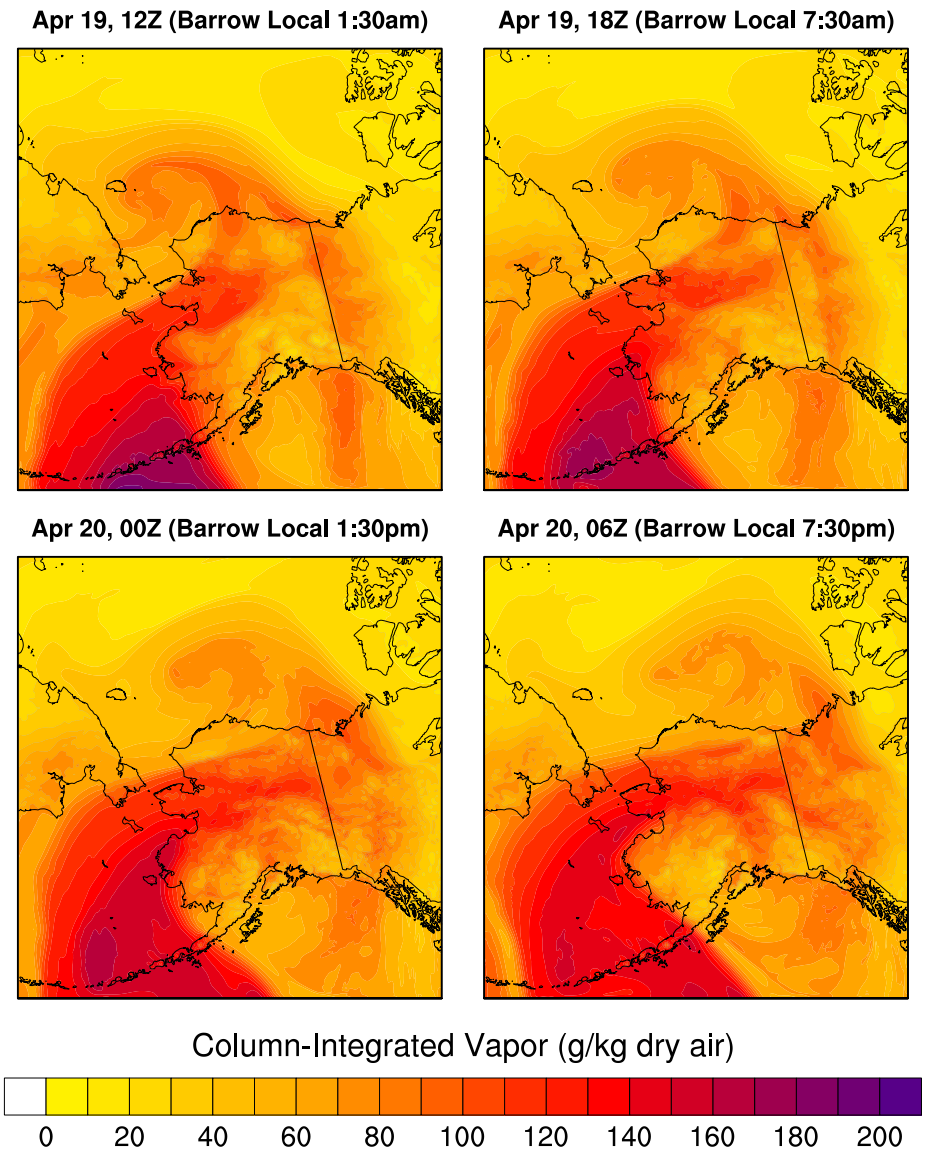

Figure 3.7: Same as Figure 3.5, except for column-integrated water vapor concentration.

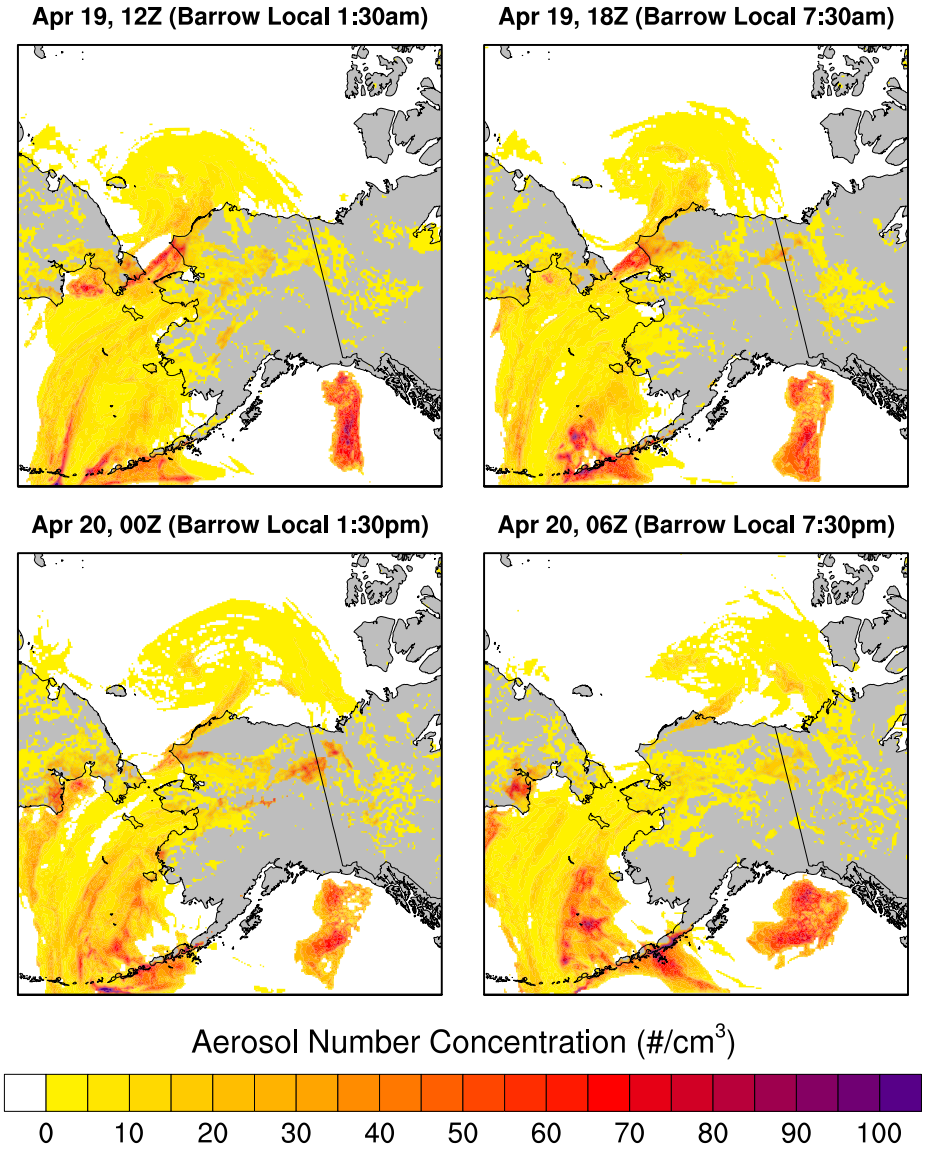

Figure 3.8: Same as Figure 3.5, except for fine aerosol number concentration of CCN (Bins 1-5).

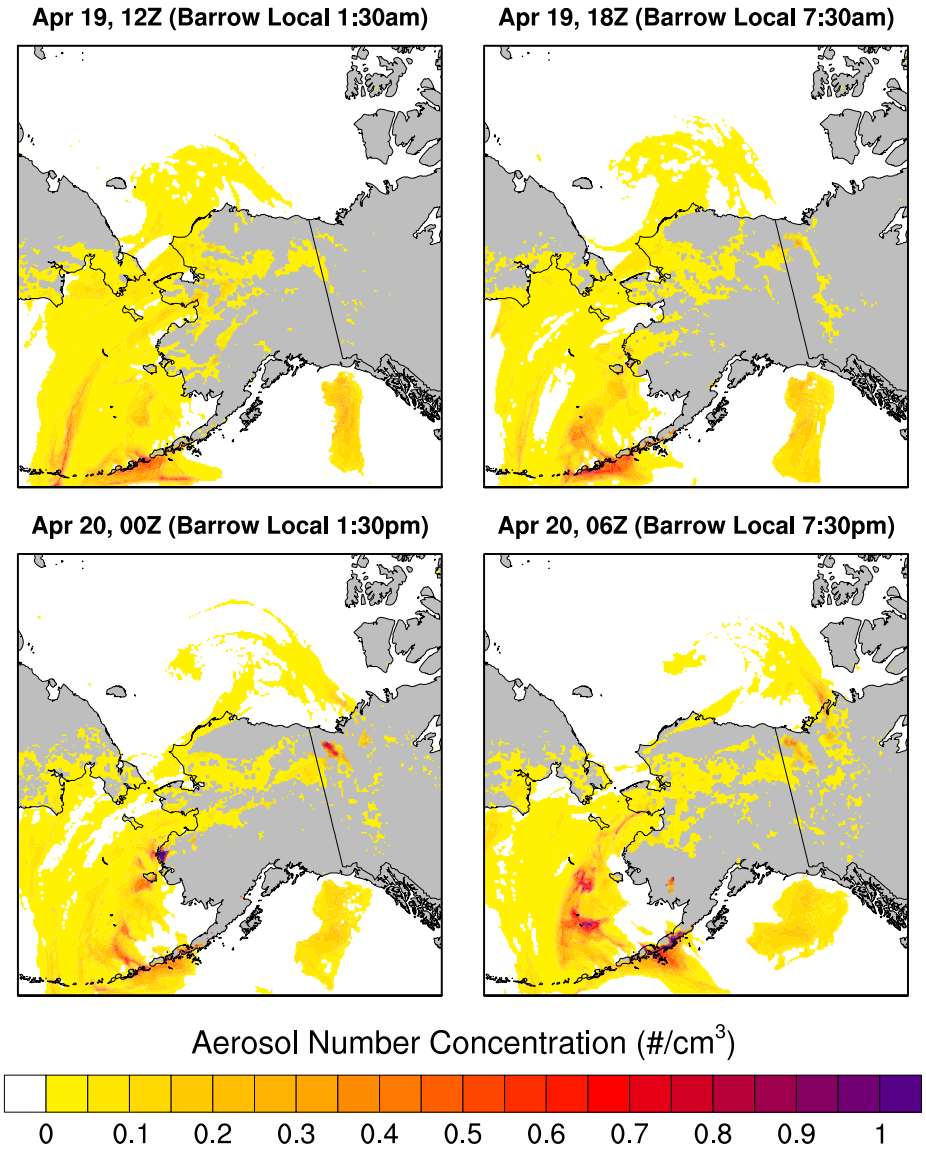

Figure 3.9: Same as Figure 3.5, except for coarse aerosol number concentration of CCN (Bins 6-8).

3.2.2 Droplet Number, Clouds, and Precipitation

The differences between the Control Run and the NoChem run, with the significance mask applied, will now be examined, beginning with the cloud droplet number. Figure 3.10 shows the locations where there is a significant difference in droplet number between the Control Run and NoChem run. These areas align particularly well with the locations of the fine aerosol CCN distribution (cf. Fig. 3.8). Note also that these areas all show an increase in droplet number, which is expected due to the increase in aerosol loading. This will enable the observance of the first aerosol indirect effect (Twomey, 1977).

With changes in droplet number come changes in cloud depth. The changes in cloud optical depth are examined in Figure 3.11. There is a marked increase in cloud optical depth in some areas with a higher in-cloud fine aerosol loading. This is consistent with the first indirect effect (Twomey, 1977). These optically thicker, brighter clouds should trigger a reduction in the shortwave radiation reaching the surface, thereby inducing a cooling surface temperature. However, there are some areas where the cloud optical depth has decreased, notably in the top left panel of Figure 3.11, which represents the simulation at midnight. This reduction in cloud optical depth is in spite of the presence of aerosols. This feature will be discussed in detail in Section 3.3, but the driving factor is the presence of coarse (>1.25 μm) aerosols.

Figure 3.12 shows the differences in precipitation between the Control Run and the NoChem run. While the locations of the precipitation changes are near to the locations of aerosol loading, the magnitude of the changes are quite small. The majority of the study area is not subject to large precipitation amounts, with available water content more of a limiting factor than aerosols. However, there is a noticeably strong increase in precipitation near the Aleutians (and co-located with the decrease in cloud optical depth) in the top left panel of Figure 3.12, again due to the presence of coarse aerosols.

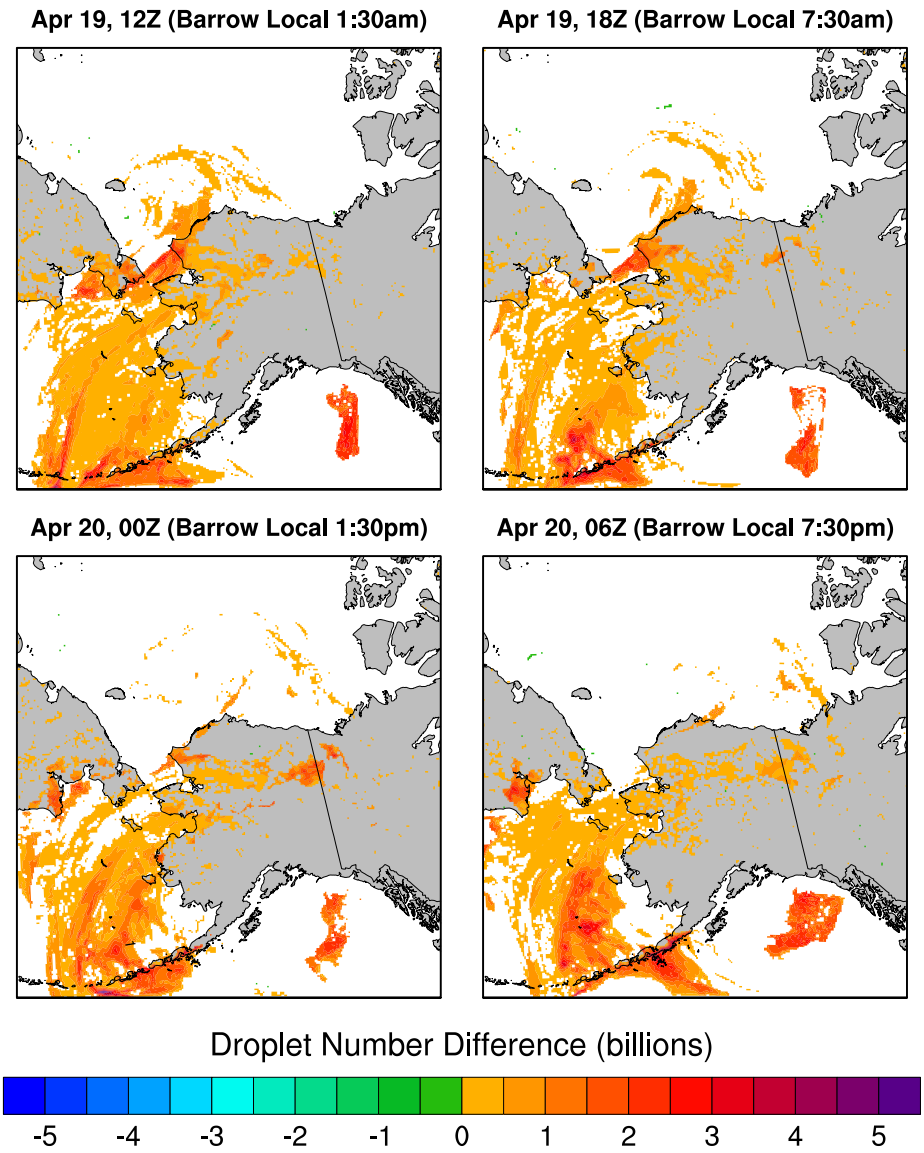

Figure 3.10: Droplet number difference between the Control Run and the NoChem run for the study area, with cells of low T value filtered out ("masked") at four different times during the diurnal cycle of April 19-20, 2008.

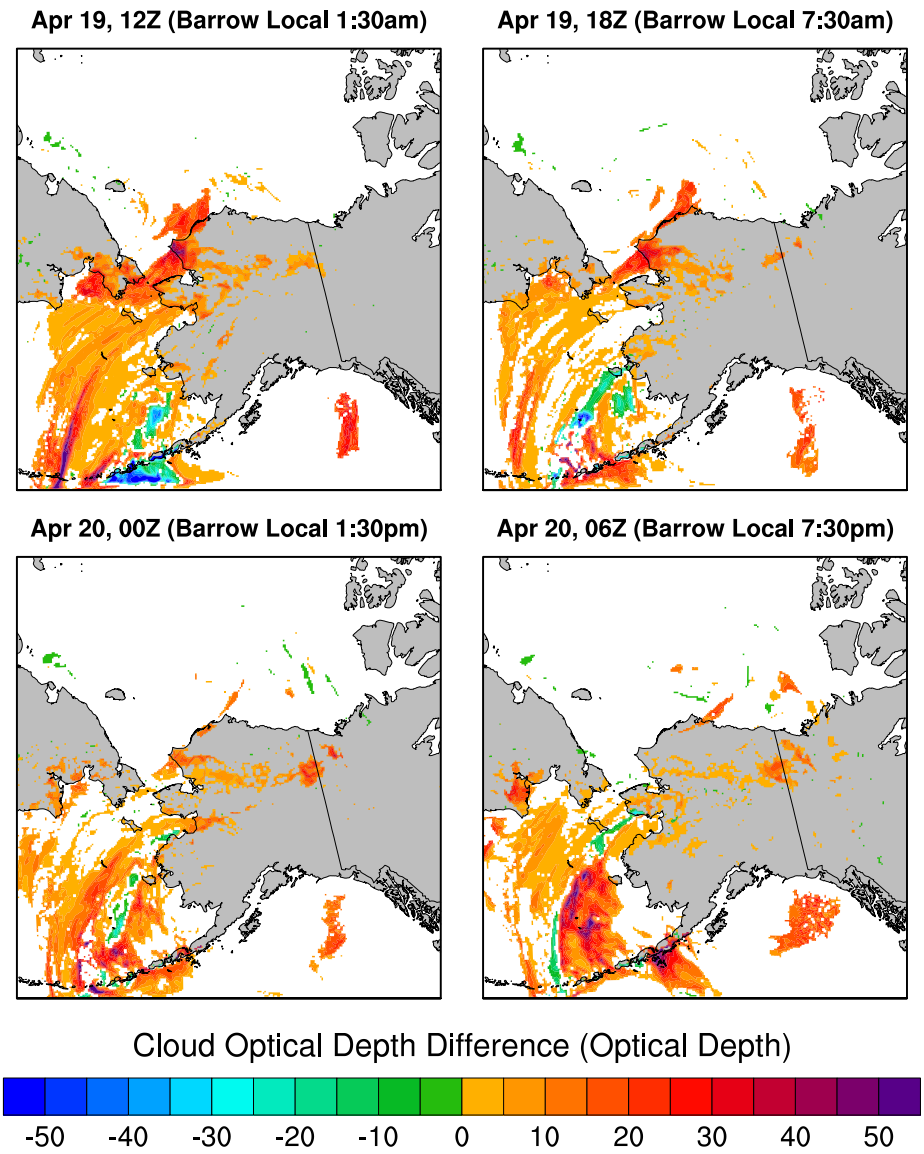

Figure 3.11: Same as Figure 3.10, except for cloud optical depth.

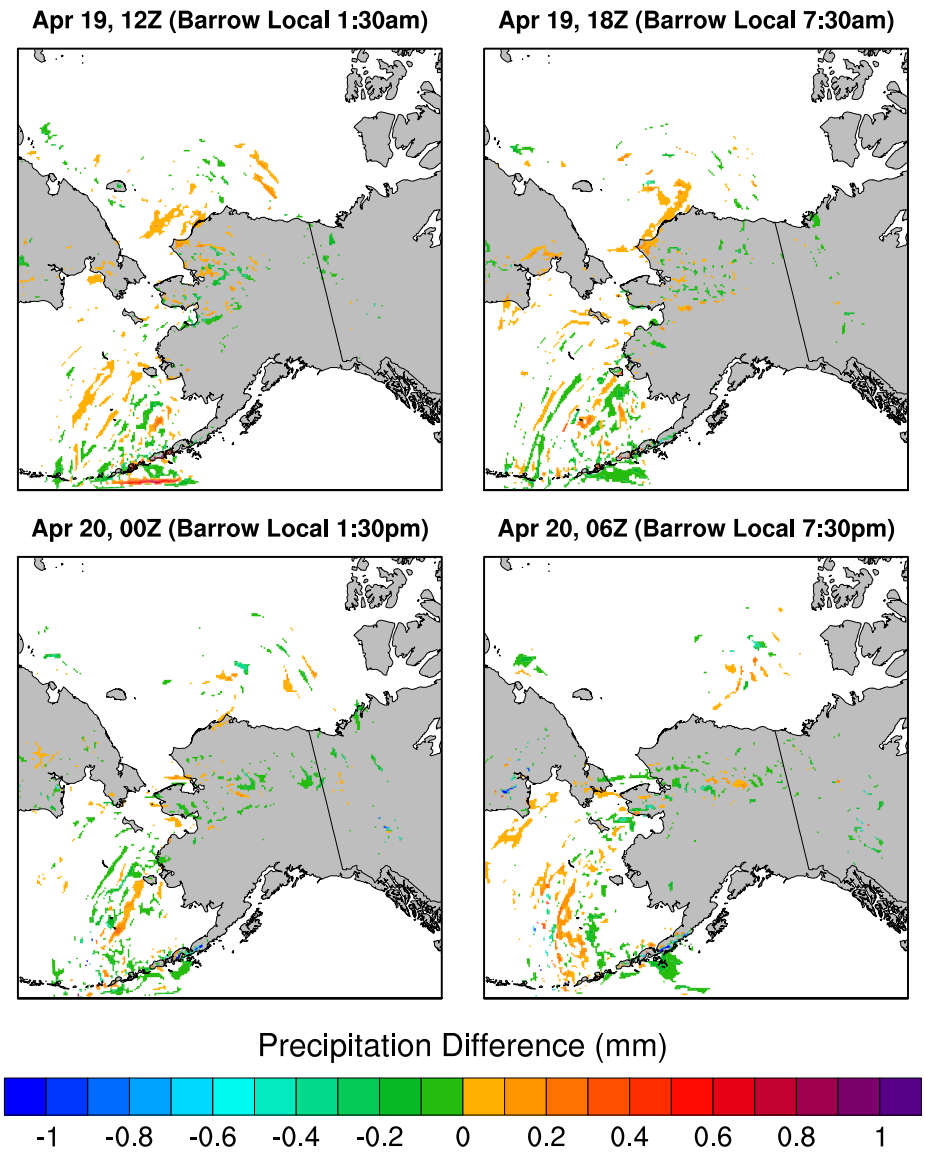

Figure 3.12: Same as Figure 3.10, except for precipitation.

3.2.3 Radiative Effects

Changes in radiative properties between the Control Run and the NoChem run are now examined. The first property to be examined is the change in downward shortwave radiation. Figure 3.13 shows the drastic decrease in shortwave radiation reaching the surface for most of the study area during the daytime. Some areas show a decrease of up to 300 W m^{-2}. The areas with the largest decreases correspond to the areas where the cloud optical depth has increased. Areas with smaller decreases correspond with areas that have relatively high aerosol loadings that are not in clouds. At other times of day, the effect is lessened due to the smaller influx of solar radiation, with there being no change at local 1:30am (top left panel of Fig. 3.13) due to the absence of solar radiation. Because of the magnitude of the difference between the Control Run and NoChem output of downward shortwave radiation, and the impact that shortwave radiation can have on the surface temperature, downward shortwave radiation is one of the major forces affecting the surface temperature.

Downward longwave radiation also plays a key role as a heat source for the surface temperature, particularly at night when the shortwave radiation is negligible. The panels of Figure 3.14 show the changes in downward longwave radiation at various times of day for the study area (the majority of the changes are also co-located with changes in clouds). Most of the differences represent an increase in downward longwave radiation for the Control Run, as an increase in cloud presence will increase the longwave radiation reaching the surface. In addition, the magnitude of the changes and the effect that downward longwave radiation can have on the surface temperature means that downward longwave radiation is also one of the major forces driving the surface temperature.

In contrast to the downward longwave changes, the changes in upward longwave Radiation are somewhat smaller in magnitude, particularly during the daytime. Figure 3.15 shows a decrease in upward longwave over most land areas during the day and at night. Over sea ice, decreases of upward longwave during the day contrast with increases at night.

These decreases/increases in upward longwave are a direct consequence of cooling/warming in the surface temperature. However, the reduction/increase in upward longwave will inhibit further cooling/warming at future time steps. This feedback loop is critical for maintaining the surface temperature. The majority of total longwave changes are due to changes in the downward longwave radiation. This is consistent with the earlier assessment of an increase in cloud optical depth, which results in both a decrease in downward shortwave radiation and an increase in downward longwave radiation, though the magnitude of the shortwave decrease is much larger, and is somewhat balanced by the change in upward longwave. The bottom left panel of Figure 3.16 shows an increase in the net longwave radiation balance at the surface in approximately the same areas as the higher decreases in downward shortwave radiation (c.f. Fig. 3.13).

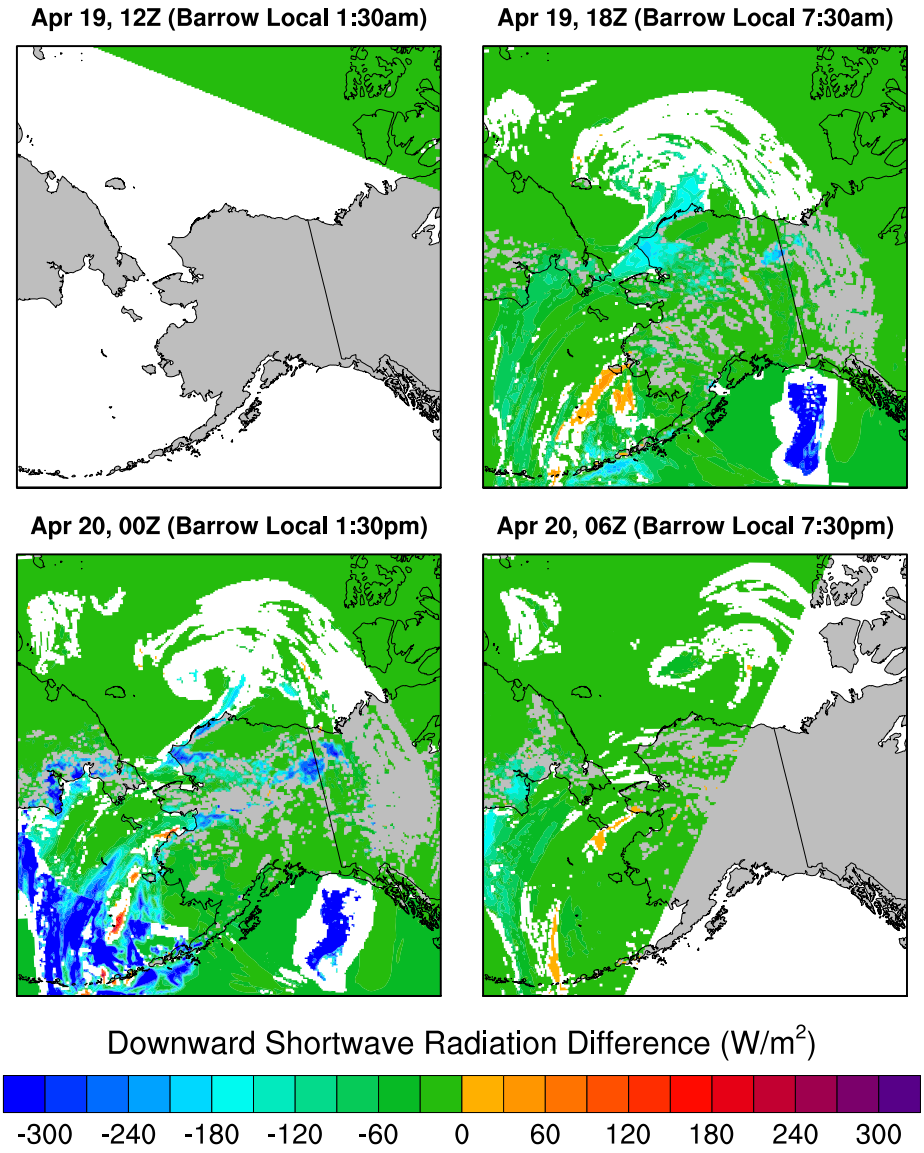

Figure 3.13: Same as Figure 3.10, except for downward shortwave radiation.

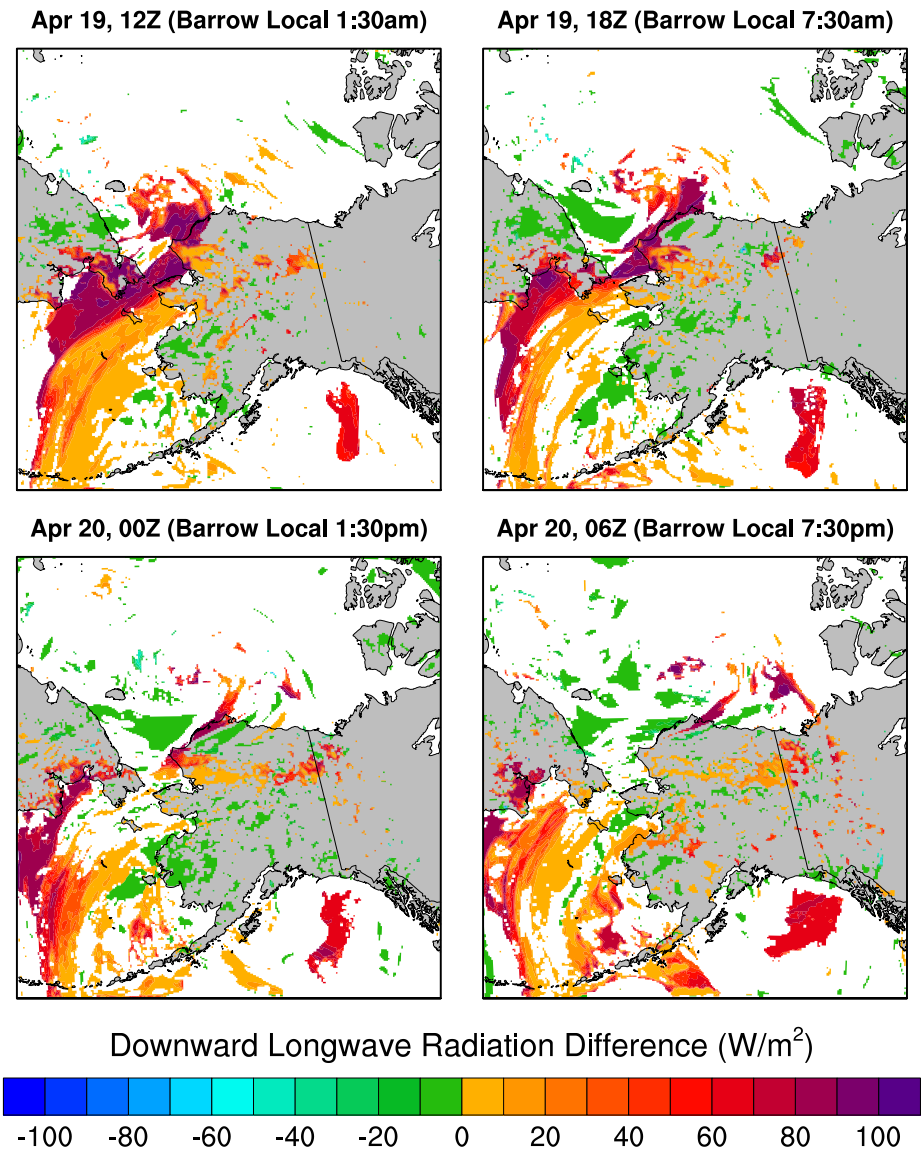

Figure 3.14: Same as Figure 3.10, except for downward longwave radiation.

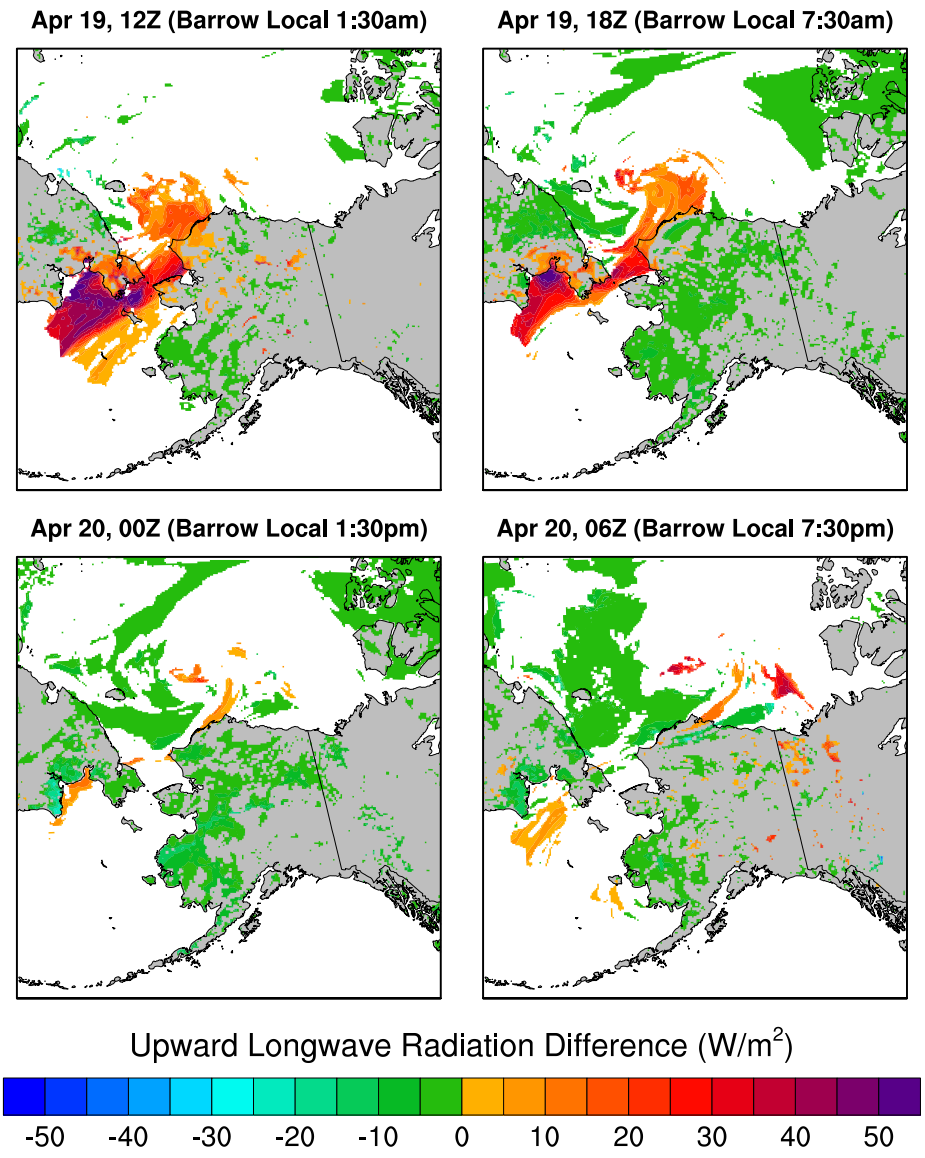

Figure 3.15: Same as Figure 3.10, except for upward longwave radiation.

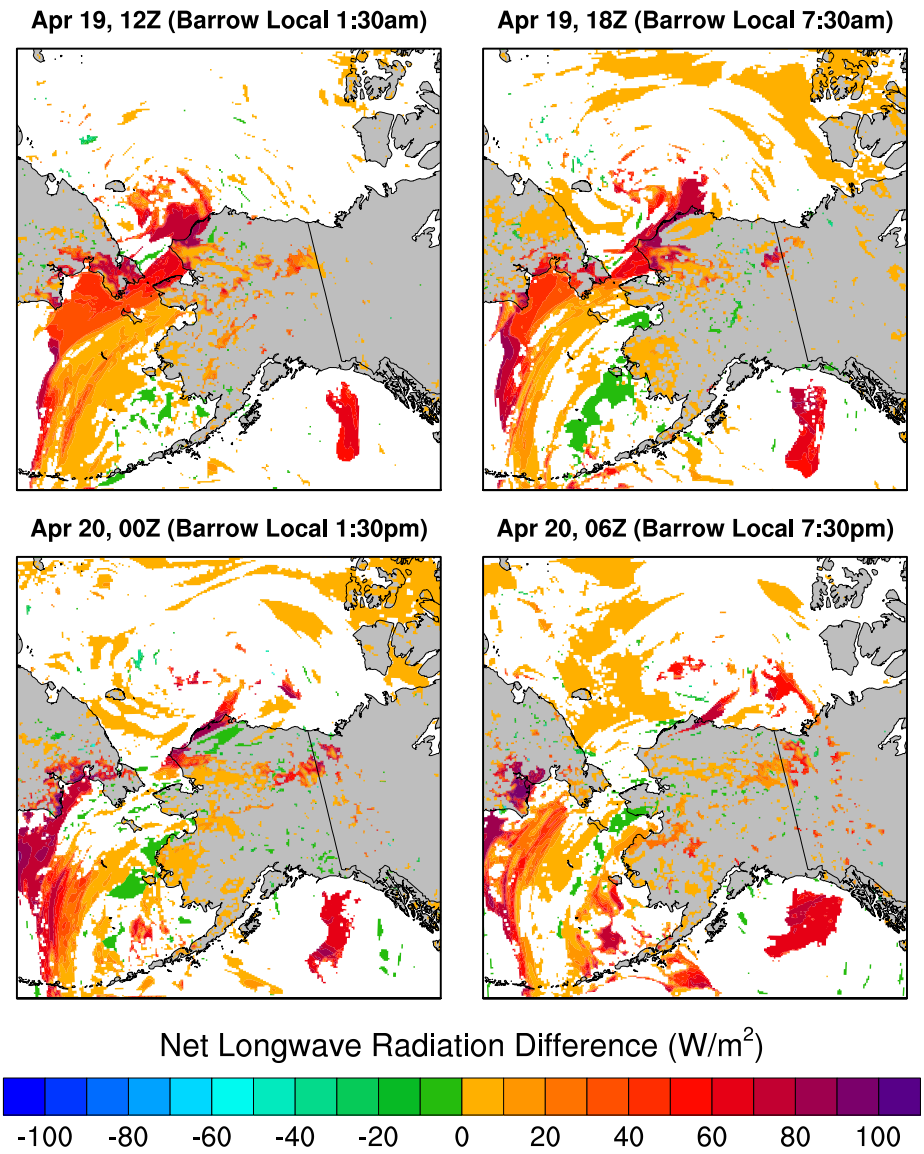

Figure 3.16: Same as Figure 3.10, except for net longwave radiation.

3.2.4 Heat Fluxes

This section examines the changes in the various heat fluxes that result from the differences between the Control Run and the NoChem run. Figure 3.17 shows a mixture of increases in sensible heat flux (i.e. increased flux from the surface to the atmosphere) over open ocean (at all times of day) with decreases in sensible heat flux over land (mostly during the daytime). The decreases of sensible heat flux over land are consistent with a decrease in surface temperature at that time period. Figure 3.18 exhibits a similar pattern for the latent heat changes, with stronger decreases over land during the day and weaker increases over open ocean at all times when compared to the sensible heat flux changes. This is again consistent with a surface cooling. Figure 3.19 shows an increase of heat flux into the surface from below ground during the day, with a slight decrease in flux at night, which again is an indication of a cooling surface temperature. This results in a weaker surface-air temperature gradient and a stronger surface-soil temperature gradient during the day, while at night the surface-air temperature gradient is stronger while the surface-soil temperature gradient is weaker.

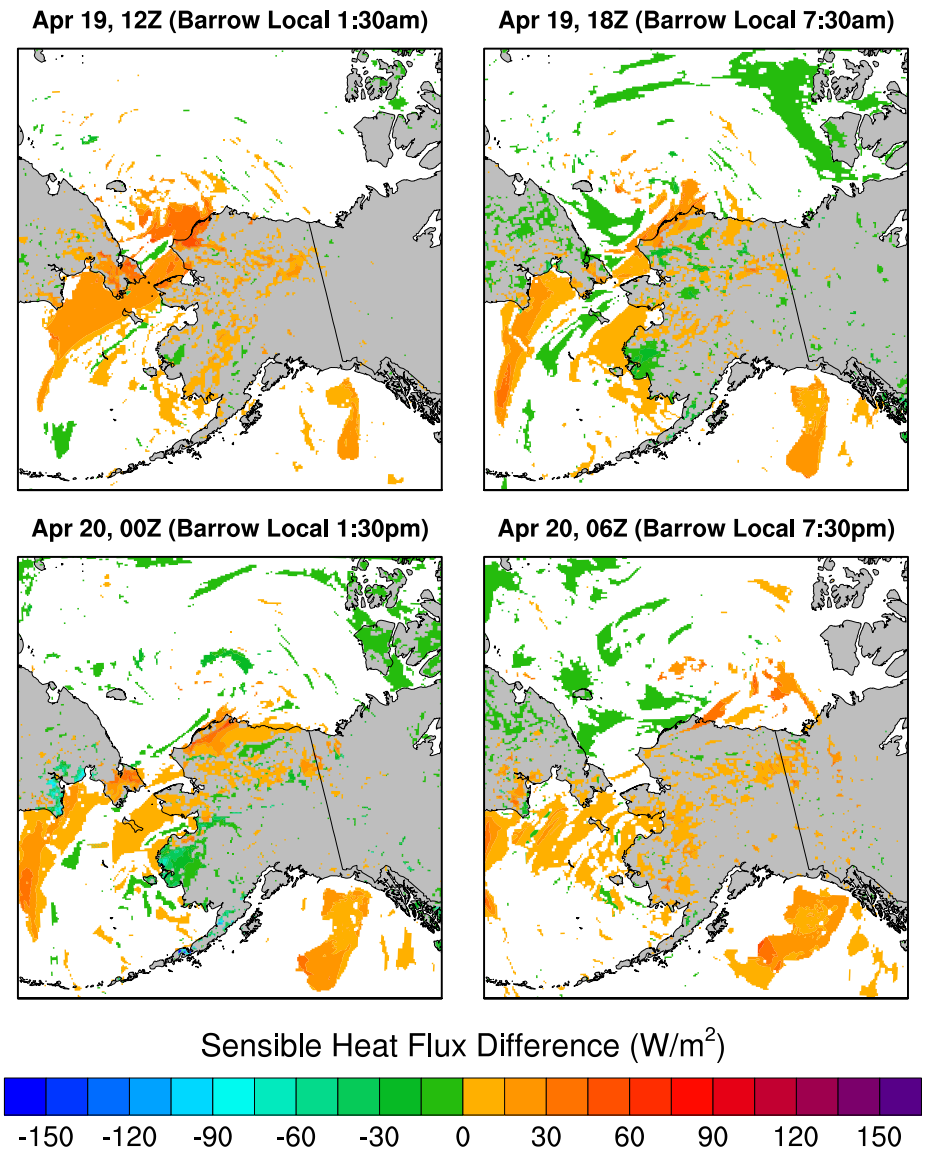

Figure 3.17: Same as Figure 3.10, except for sensible heat flux.

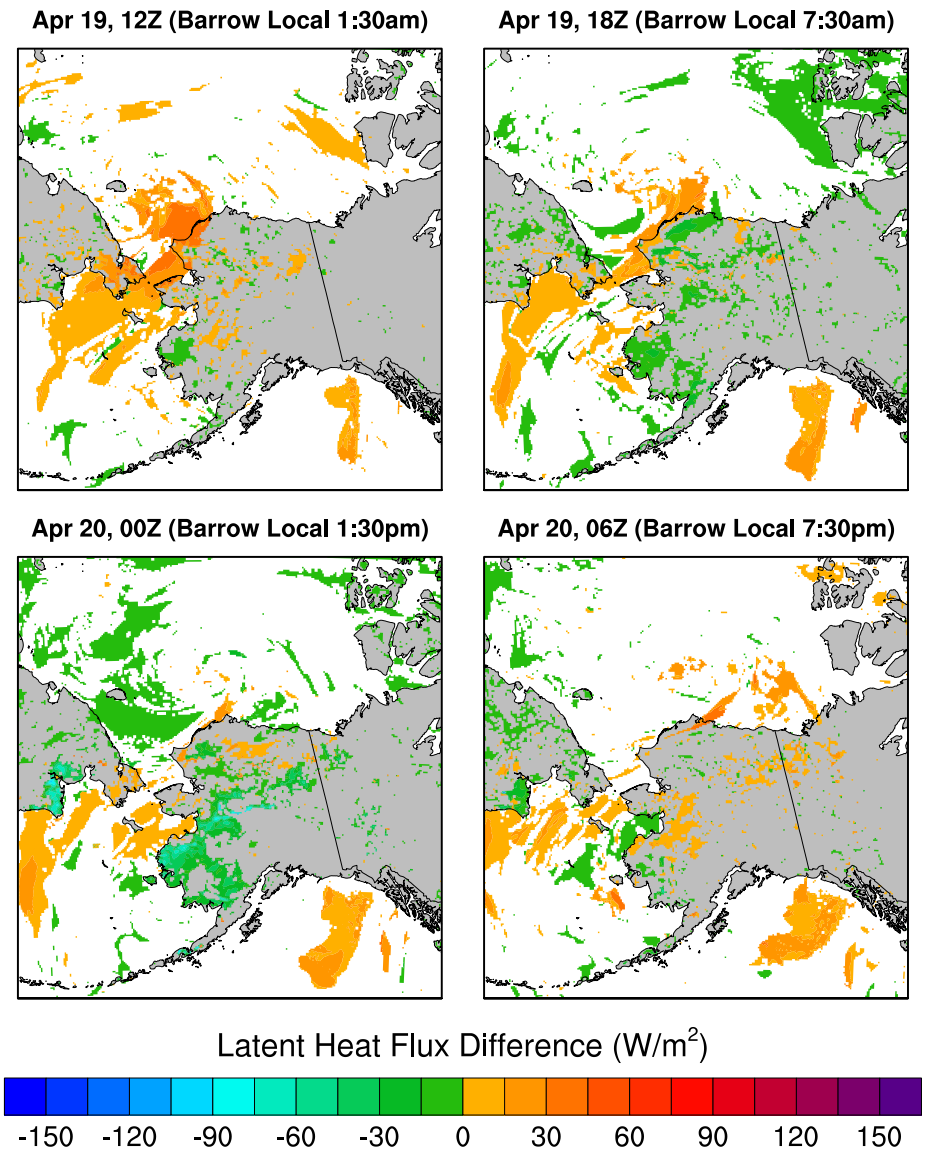

Figure 3.18: Same as Figure 3.10, except for latent heat flux.

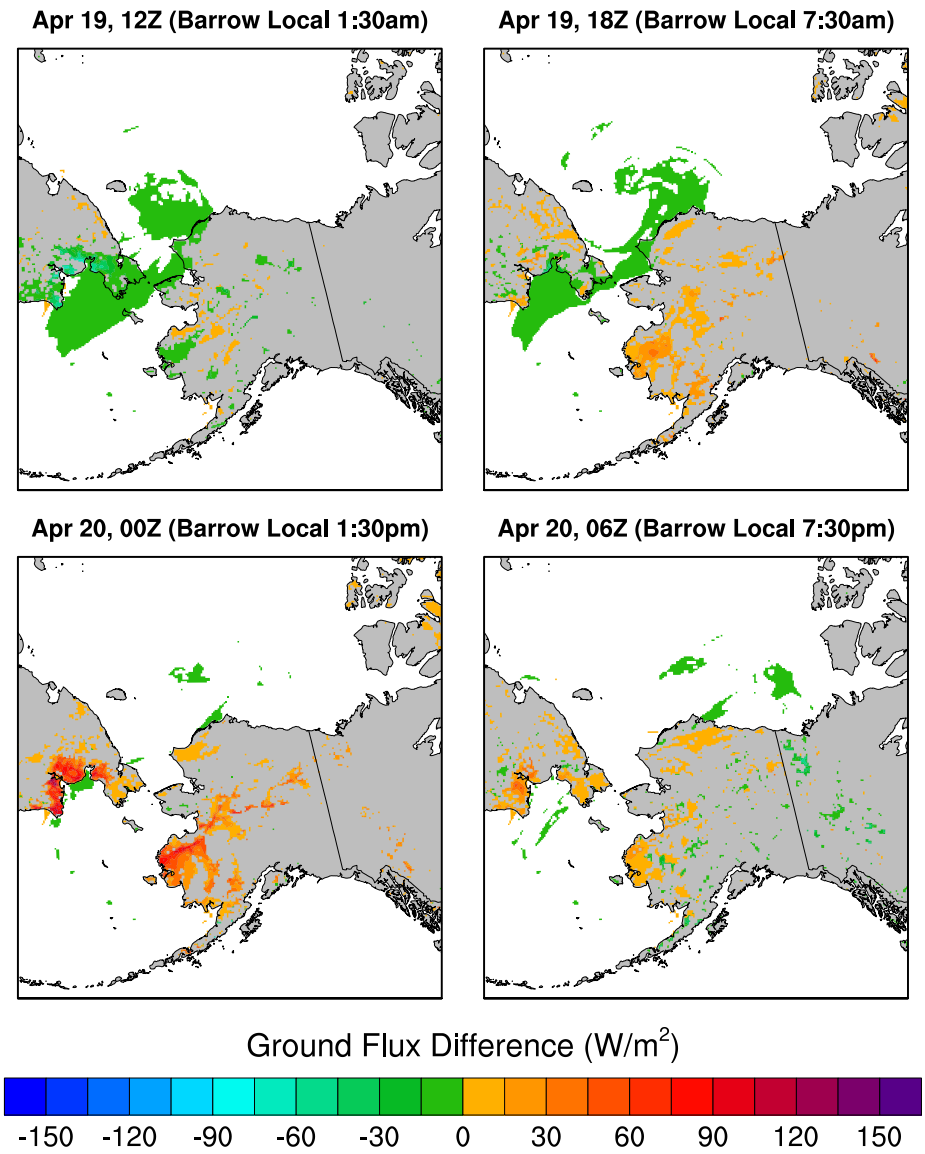

Figure 3.19: Same as Figure 3.10, except for ground flux.

3.2.5 Other Changes

Changes in other parameters will be explored in this section. These entities are not as influential as the radiative parameters, but they may indicate changes to the surface temperature on a local scale. The first figure shows the changes in planetary boundary layer (PBL) height over the study area. Figure 3.20 shows a general increase in PBL height over the areas of strong aerosol presence, particularly at night. However, there is a decrease in PBL height over some land areas during the day. These changes are again consistent with a cooling surface temperature during the day.

The subsequent figure shows the changes in snow depth for the study area (Fig. 3.21). The interesting thing to note is the near universal increase in snow depth from the Control Run compared to the NoChem run at all times of day. This is consistent with the reduction in downward radiation and the general surface cooling during the day, though it seems whatever night-time warming is present is having little effect on the snow depth. It should be noted that these changes are occurring in April, and as such likely represent a reduction in melting rather than an increase in snow formation.

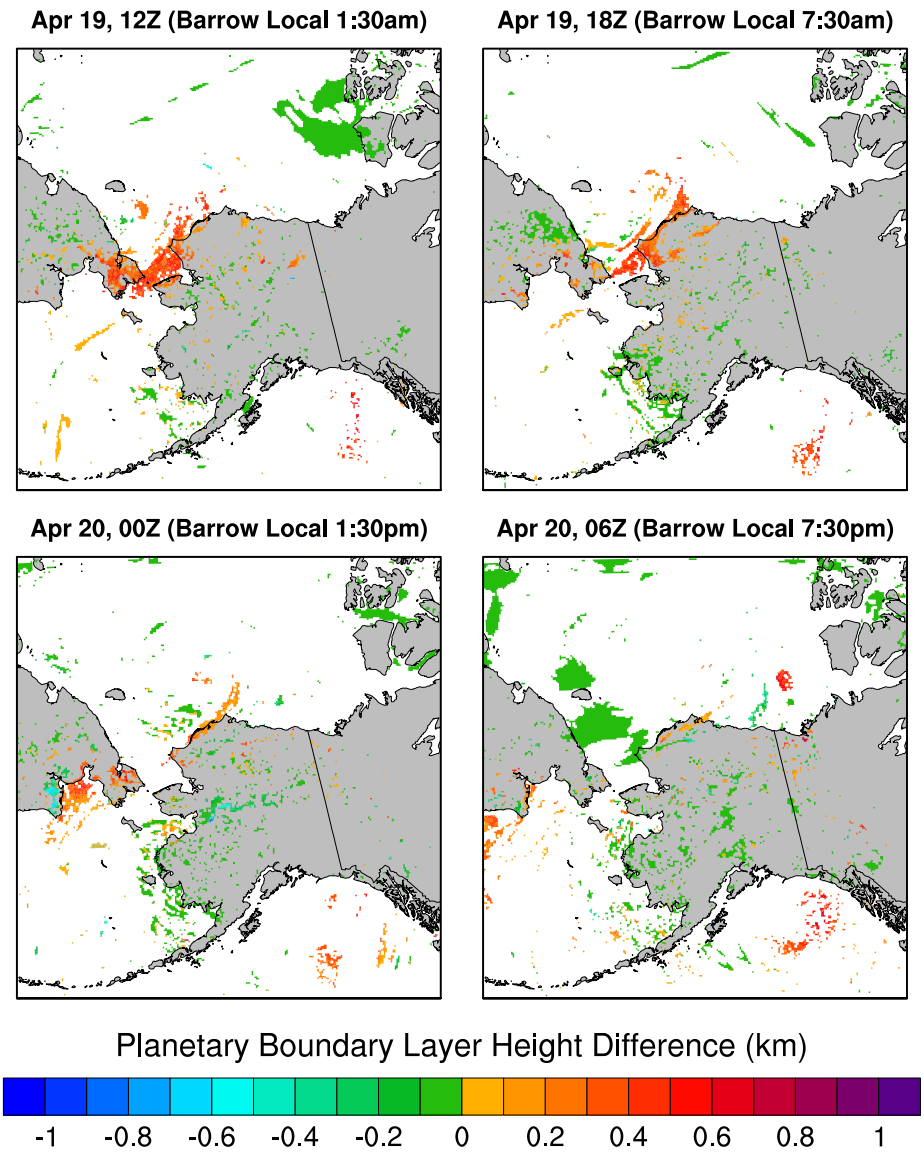

Figure 3.20: Same as Figure 3.10, except for planetary boundary layer height.

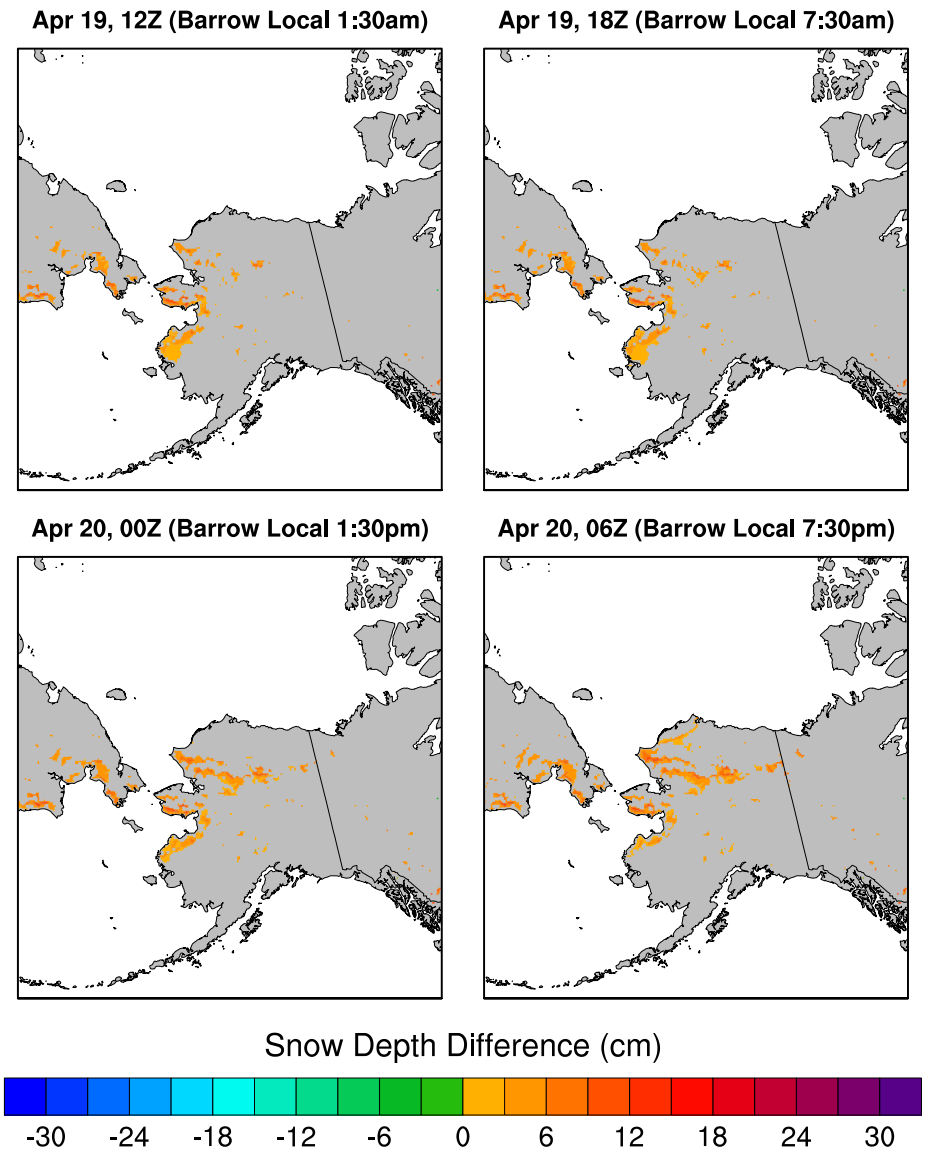

Figure 3.21: Same as Figure 3.10, except for snow depth.

3.2.6 Temperature

The surface temperature changes are shown in Figure 3.22. The majority of the surface temperature changes during the day are negative, with a particularly strong signal over land, which is indicative of daytime surface cooling. The contrast to the warming at night is quite strong, as shown in the top left panel, where there is a strong signal over sea ice. Although the sea surface temperature (SST) is specified in these model runs, due to the large heat capacity of water, open water surface temperatures during the diurnal cycle are likely not affected by aerosols. During day-time, both land and sea ice areas experience an overall cooling due to aerosol indirect effects of up to about 2-3 °C, largely as a result of an increase in upward longwave radiation as well as a decrease in downward shortwave radiation. Note that the largest cooling takes place over land. During night-time, increases in downward longwave radiation due to aerosol indirect effects, particularly over sea ice, have indicated a strong warming signal, up to about 2-3 °C. These results suggest that the contrast between changes during the day and changes at night are large, particularly when examining the effects over different surface properties, such as land and sea ice. The relative magnitudes of shortwave and longwave radiation changes can cause night-time warming over ice areas, while causing day-time cooling over both land and sea ice surfaces.

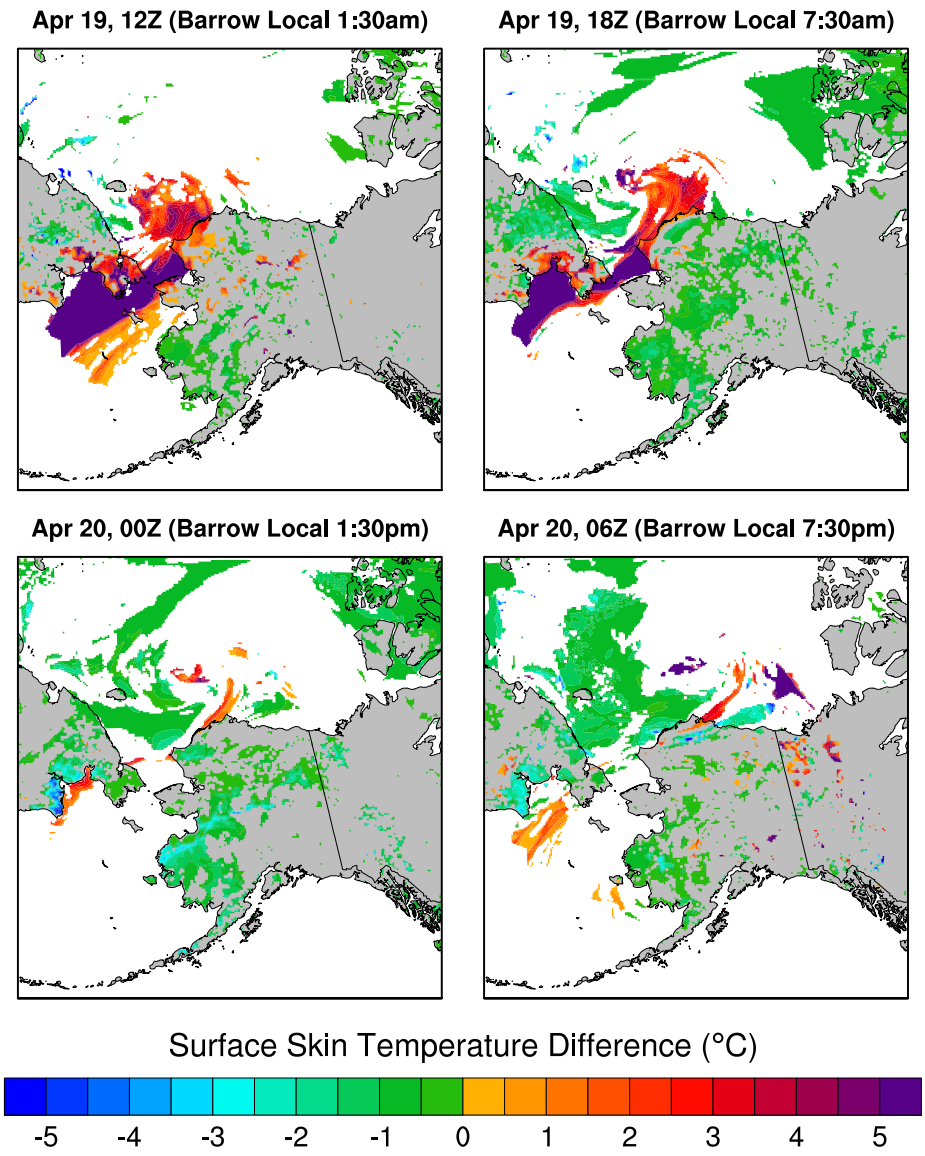

Figure 3.22: Same as Figure 3.10, except for surface temperature.

3.3 Separating Aerosol Effects

While Section 3.2 examined the total aerosol effect on the domain, Section 3.3 will examine the contributions of each aerosol effect (i.e., the direct effect, the semi-direct effect, and the indirect effects) to the total aerosol effect. This is accomplished by examining the differences between several model runs as described in the methodology section. The direct effect is measured by the difference between the Control Run (which simulates the direct, semi-direct, and indirect effects) and the NoAerRad run (which simulates the semi-direct and indirect effects). The semi-direct effect is the result of the difference between the Control Run and the BC0 run (which simulates the direct and indirect effects, but not the semi-direct effect). The indirect effects are the result of the difference between the the NoAerRadorBC run (which simulates only the indirect effects) and the NoChem run (which does not simulate any aerosol effects). Note that the 95% confidence level calculated in 3.2 is slightly higher for indirect effects, as it contains fewer ensemble members. For clarity, only the previously calculated 95% confidence level based on seven ensemble members is included in the subsequent figures.

In addition to the breakdown of the total aerosol effect into its constituent components, the domain itself may be broken into specified regions. This will allow for an examination of impacts that may be lost when averaging components filtered through the T Test over the entire domain, and will allow for a differentiation between regions that are affected by various proximate factors (such as land vs sea ice). The land regions of the domain follow the definitions as provided by the State of Alaska and by accepted international boundaries. The five land regions are Russia, The Far North of Alaska, the Interior of Alaska, Southwest Alaska, and South Central Alaska. The region encompassing the portion of the domain covered by sea ice (cf. Fig. 2.1) is also examined. To ascertain the relative impacts of the various aerosol effects on surface energy balance components and surface temperature, these components are averaged over two out of the six regions: the sea ice region,

where a large portion of warming was shown in Section 3.2, and Southwest Alaska, which is representative of the changes over land where the largest aerosol effect on temperature is seen (cf. Fig 3.22). These two regions will contrast the two different surface characteristics in the domain (i.e., sea ice and land). While the other land regions were also examined, their results were similar to Southwest Alaska and are not pictured. These components are then plotted against time for the entire analysis period of April 18th to April 21st, 2008.

The following plots will show the average change of each component over the region for the aerosol direct effect, semi-direct effect, and indirect effects. In addition, the 95% confidence level lines are shown. If the change in the component is between the two confidence lines, then it is considered noise (i.e., could be a combination of aerosol effect and/or meteorological variability). If the change in the component is above both confidence lines or below both confidence lines, then it is not considered noise and is indicative of the change wrought by the aerosol direct effect, semi-direct effect, or indirect effects.

The first components to be explored have to do with clouds, and are shown in Figure 3.23. The droplet number changes for both sea ice and Southwest Alaska are due almost exclusively to the aerosol indirect effects, with a total effect average increase of 250 million and 450 million, respectively. These results are somewhat expected, as the increase in droplet number due to aerosols is the very definition of the first indirect effect. The cloud optical depth changes are also dominated by the indirect effects. Again, this is as we would expect given the definition of the first indirect effect. However, there is a significant decrease in cloud optical depth in the middle of the analysis period for Southwest Alaska. An explanation for this seemingly counter-intuitive result is found in the influence of the size distribution of aerosols. The concept behind the indirect effects is that aerosols inhibit precipitation by distributing the same amount of liquid water in a cloud onto an increased number of CCN. This results in an increase in time for droplets to grow to the appropriate size for precipitation. However, this is based upon the premise that the aerosol sizes are

small (less than 1.25 μm, or "fine" particles). Aerosols larger than 1.25 μm, or "coarse" particles, enhance precipitation efficiency by being of sufficient size to ease the transition from cloud droplet to rain drop (Kogan et al., 2011). Therefore, in the presence of coarse aerosols, precipitation will be enhanced, and cloud cover reduced. Southwest Alaska contained a large aerosol loading of both fine and coarse particles (cf. Figs. 3.5 and 3.6), with the higher concentration of coarse particles resulting from the proximity of the region to open ocean, wherein larger aerosols, such as sea salt, are readily formed. This precipitation enhancement for Southwest Alaska is shown in the bottom right panel of Figure 3.23. There is also a very small increase in the overall precipitation over sea ice.

The aerosol effects on the radiative components are examined in Figure 3.24, in which the average radiation for the simulation domain has been plotted for the analysis period. During the analysis period, the reduction in downward shortwave radiation over sea ice of 40-70 Wm^{-2} is highly dependent on the diurnal cycle, with the difference due to aerosol effects eliminated when there is no solar radiation over the domain (as one would expect). The semi-direct effect contributes least to the overall effect due to low black carbon concentration. The direct effect on radiation is noticeably larger, with a reduction of about 15 Wm^{-2} on average. The indirect effects make up the difference with the highest reduction at 40-50 Wm^{-2}, with the increase in cloud cover preventing solar radiation from reaching the surface. The diurnal cycle of daytime cooling is stronger in Southwest Alaska than over sea ice, although the effect is somewhat mitigated in the time-frame following the reduction in cloud cover. There is an average increase of 10-15 Wm^{-2} due to the combined effects of all aerosols on downwelling longwave radiation over sea ice. In contrast to the shortwave radiation, this is not as dependent on the diurnal cycle. The semi-direct effect and direct effect contribute less than 1 Wm^{-2} of radiative forcing. The indirect effects are the driving force behind the total changes, contributing almost all of the 10-15 Wm^{-2} total increase. This increase is due to the increase in cloud cover, which emits longwave radiation to the

surface. A similar but smaller increase occurs in Southwest Alaska, with the smallest increase during a time of reduced cloud cover. The upwelling longwave radiation also displays a strong diurnal cycle. There is a large increase in upward longwave radiation over sea ice at night (which cools the surface) and a small decrease in upward longwave radiation during the day over sea ice (slightly warming the surface). Over Southwest Alaska, the day-time warming effect is larger than over sea ice, while the night-time cooling is near zero or negative. These changes are a reaction to temperature changes, as upwelling longwave radiation is driven largely by the surface temperature. The net longwave changes align well with the downward longwave changes for both regions, in that the warming due to the total aerosol effect is driven largely by the aerosol indirect effects warming.

The time series of the heat fluxes are displayed in Figure 3.25. The sensible heat flux changes over sea ice show a strong diurnal cycle, with a strong positive surface-to-air heat flux at night and little change in surface-to-air heat flux during the day. The average flux increase of 3 Wm^{-2} for the total aerosol effect has a large diurnal cycle, largely driven by the diurnal cycle of the indirect effects changes, which have an average flux increase of 3.5 Wm^{-2}. The direct and semi-direct effects are lower in magnitude, and they provide an average flux decrease of 0.5 Wm^{-2}. The latent heat flux changes are of a similar form, with the total aerosol effect having a large diurnal cycle and, like sensible heat, an average flux increase of 3 Wm^{-2}, again driven by the large diurnal cycle of the indirect effects. The ground flux changes are mostly zero, since there is little flux between the sea ice and the underlying ocean due to temperature changes. Note that all of these changes over sea ice are significantly smaller than the changes in radiative fluxes. The heat fluxes over Southwest Alaska show a marked contrast to the effects over sea ice. While there were large increases in both sensible and latent heat fluxes at night over sea ice, and mild decreases during the day, the night-time heat flux changes over Southwest Alaska are effectively zero, while the daytime flux decreases are quite strong. Since the changes in sensible and latent heat fluxes track the changes in surface temperature, this would suggest an overall cooling effect in

Southwest Alaska, with a strong diurnal component.

The changes in surface temperature are shown in Figure 3.26. Over the sea ice, the Control Run is warmer than the NoChem run by an average of 0.5 °C at night for the analysis period. This warming has been further partitioned into changes as a result of the direct effect (cooling of 0.25 °C), the semi-direct effect (warming of 0.05 °C), and the indirect effects (warming of 0.7 °C). The semi-direct effect is below the 95% confidence level due to low black carbon concentration, the direct effect exceeds the 95% confidence level during the day, and the indirect effects exceed the 95% confidence level during both day and night. This suggests that the semi-direct effect on surface temperature is somewhat small, while the direct effect cooling brings the total temperature effect down during the day. It is interesting to note that the indirect effects have a net warming effect over sea ice. With aerosols increasing cloud depth, the clouds not only block radiation during the day, but also give off more longwave radiation at night. This longwave indirect effect is stronger than the indirect effect on solar radiation for the sea ice portion of the domain. However, this relationship does not hold over Southwest Alaska, where a strong day-time cooling combines with a slight cooling at night, resulting in an overall cooling over the region.

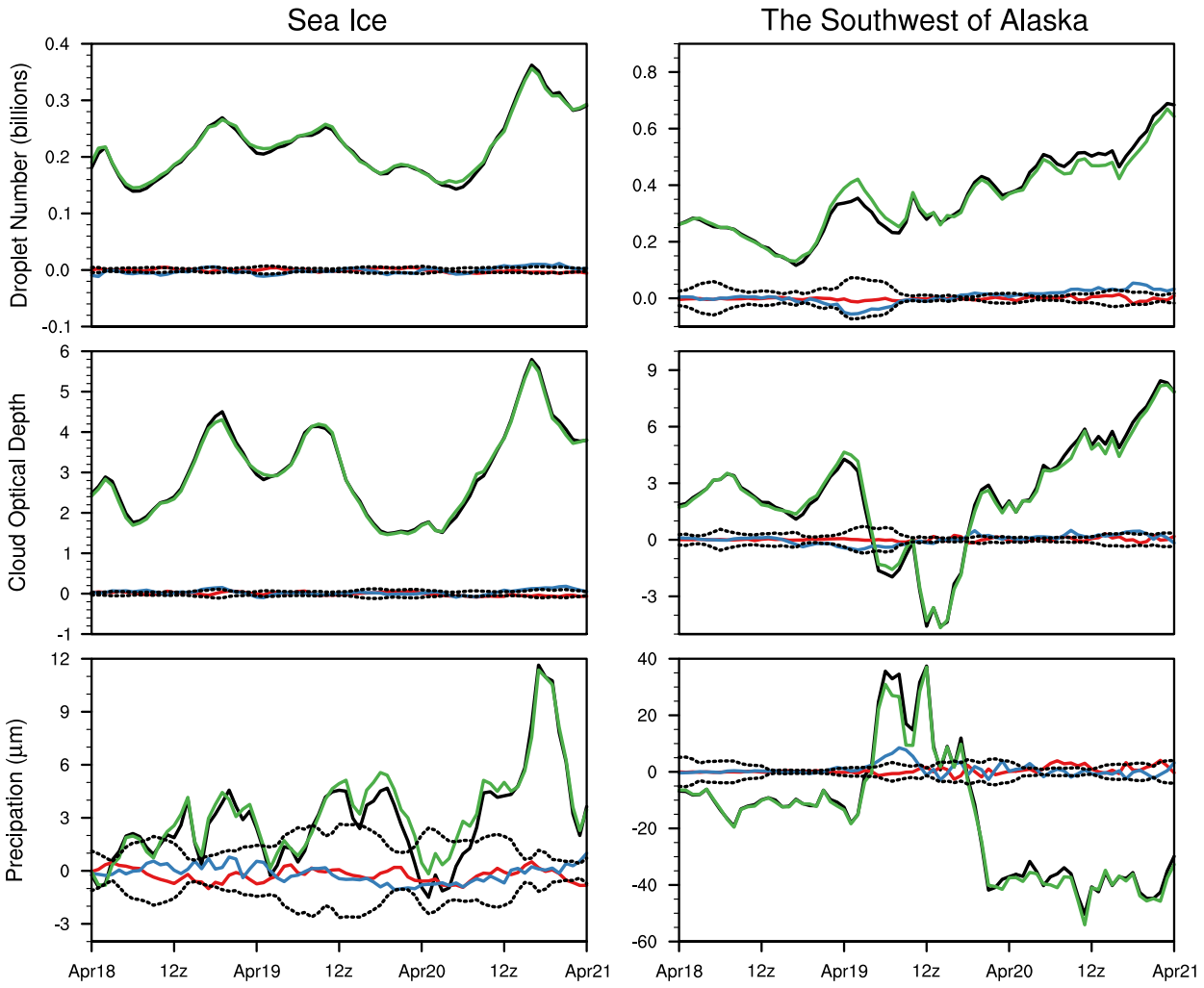

Figure 3.23: Droplet number (top), cloud optical depth (middle), and precipitation (bottom) changes broken down by aerosol effect over the sea ice (left column) and Southwest Alaska (right column) for the period April 18th to April 21st. The total aerosol effect (black), direct effect (red), semi-direct effect (blue), and indirect effects (green) are shown with the 95% confidence interval (dashed black).

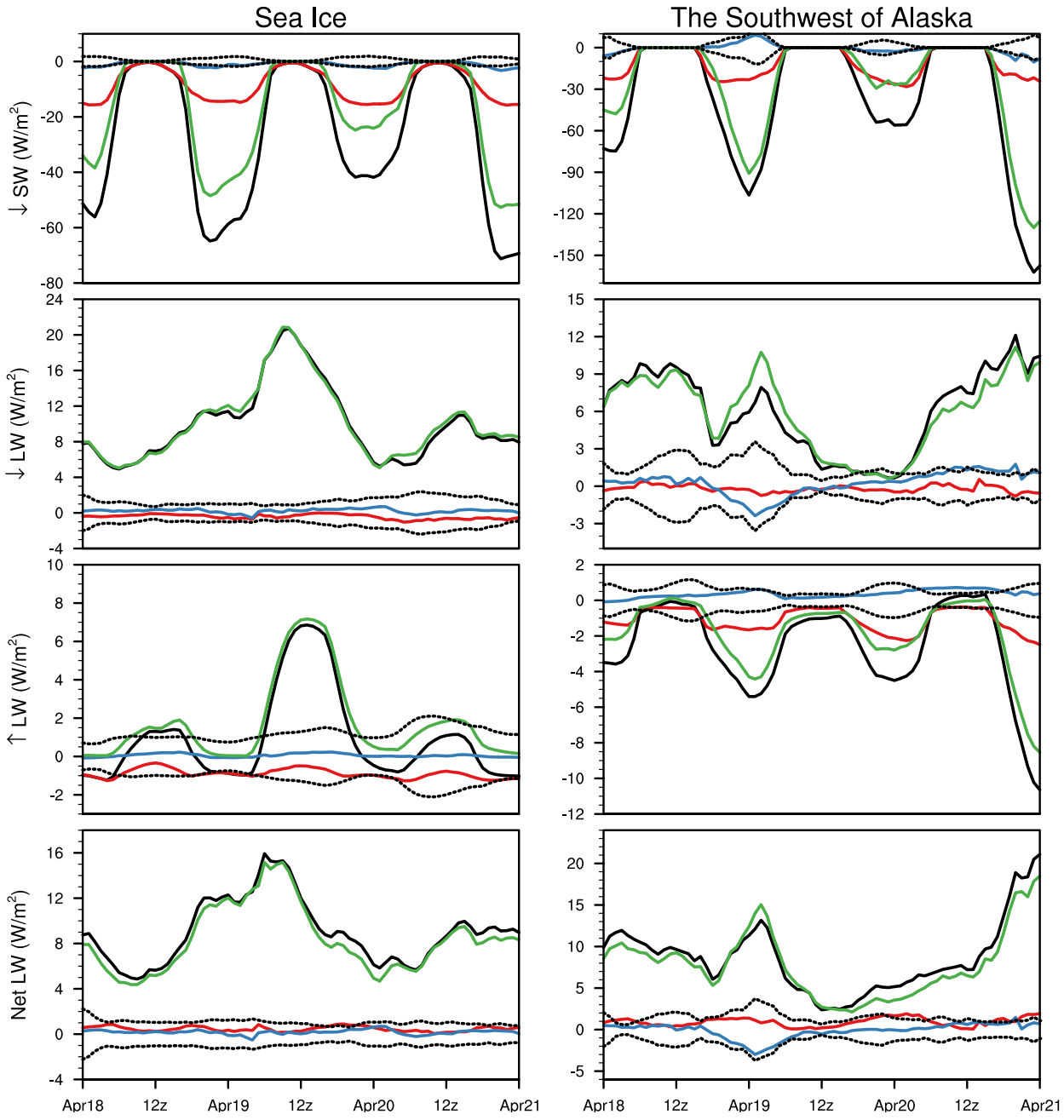

Figure 3.24: Same as Figure 3.23, except for downward shortwave radiation (top), downward longwave radiation (second), upward longwave radiation (third), and net longwave radiation (bottom).

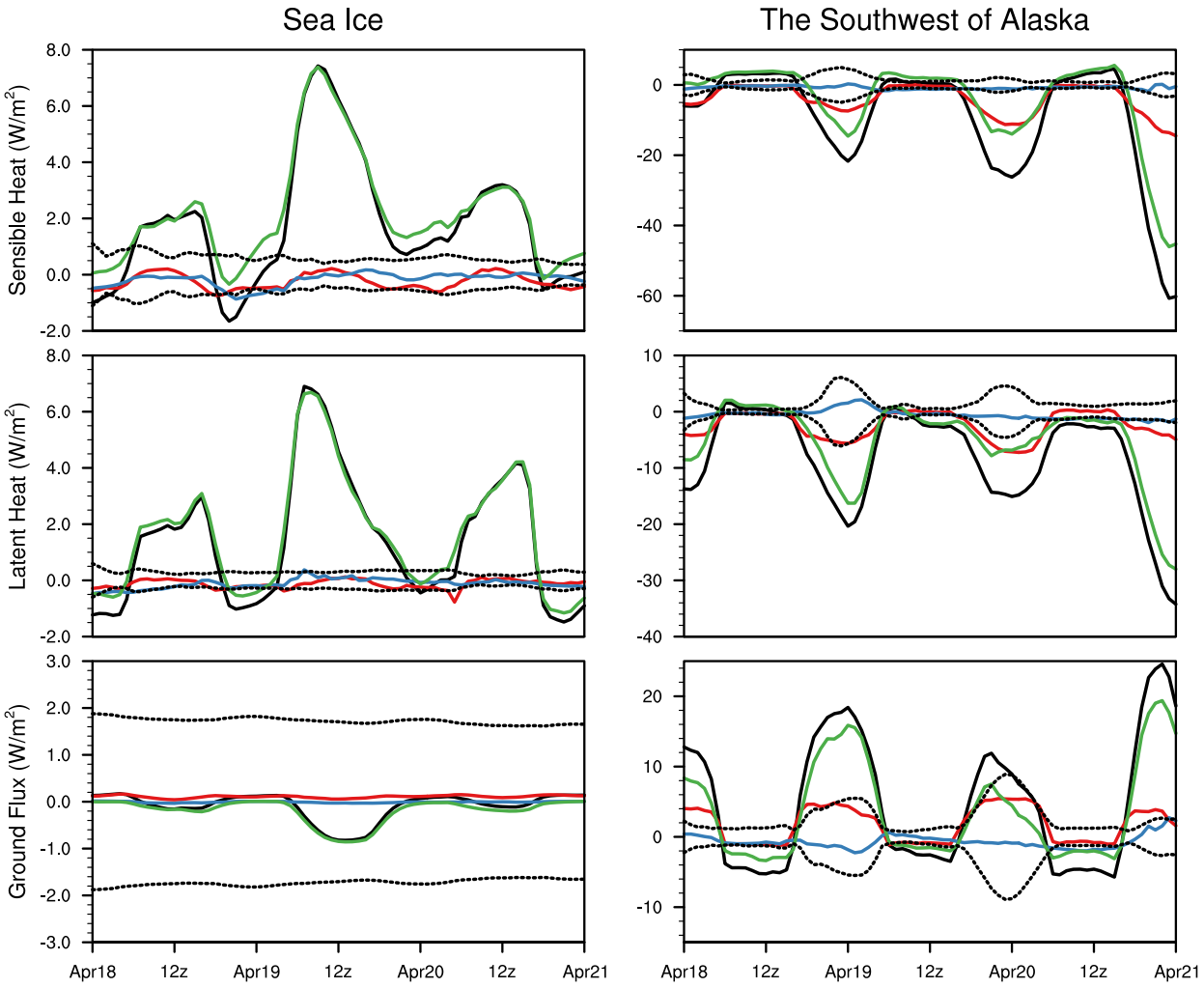

Figure 3.25: Same as Figure 3.23, except for sensible heat flux (top), latent heat flux (middle), and ground flux (bottom).

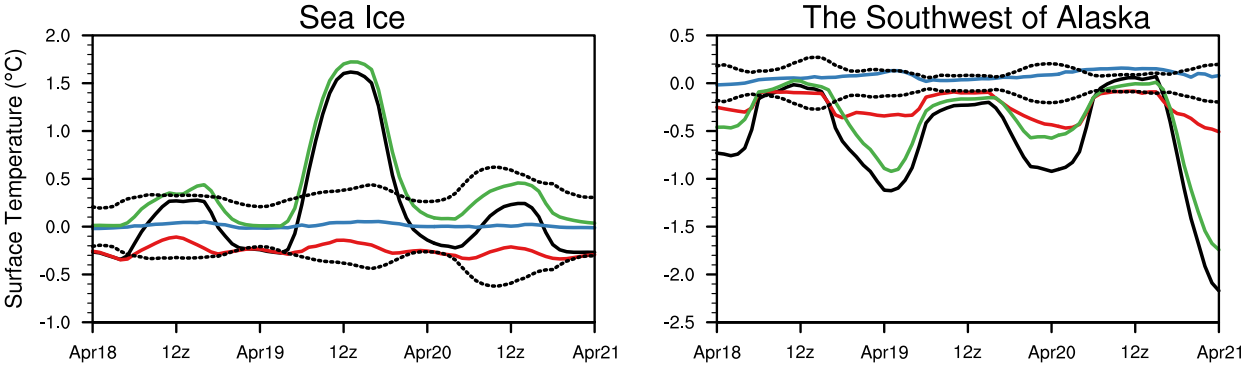

Figure 3.26: Same as Figure 3.23, except for surface temperature.

Chapter 4: Conclusions

4.1 Summary

The surface skin temperature diurnal cycle is an important element of the Arctic climate system and shows a strong annual variation. The Arctic sea ice cover has been in decline since the 1950s. This decline is more pronounced in the spring and summer months and recent years have produced striking record minima. As a result, the most sensitive region to global warming caused by increasing greenhouse gases is over the Arctic. From the observations of recent years, however there is still not enough evidence to draw the conclusion of the Arctic warming as most GCMs suggested. The high surface albedo of snow and ice, and the unique atmospheric aerosol composition (mostly dominated by sulfate aerosols and sea salt), make the Arctic climate system very sensitive to the external forcing (e.g., aerosol-cloud-radiation feedback). These external forcings need to be studied to improve our understanding the Arctic climate system, particularly during the diurnal cycle.

In this study, we use the WRF-CHEM model to examine the aerosol effects on the Arctic skin surface temperature during the diurnal cycle. This study shows that the aerosol effects on skin surface temperature will vary during the diurnal cycle, depending upon aerosol loading, available moisture, and underlying surface thermal properties (e.g., open ocean, sea-ice, and land surfaces). This study also shows that the surface temperature changes are due almost exclusively to the indirect aerosol effects, which mostly cause strong warming over sea-ice regions during night-time and cooling over land regions during the diurnal cycle, while over the open ocean, the large heat capacity of water removes the prospect of surface temperature changes due to aerosols.

Over sea ice regions, the surface temperature increases at night throughout the simulation time period by about 0.5 °C, with the maximum surface temperature increase (about 1.5 °C) occurring on the night of April 19th, 2008 and the maximum surface temperature decrease (about -0.3 °C) occurring during each day of the simulation period. On the contrary, over land regions, the average surface temperature decreases throughout the simulation time period during the day by about -1.0 °C, with the maximum surface temperature increase (less than 0.1 °C) occurring on the night of April 20th, 2008 and the maximum surface temperature decrease (about -2 °C) occurring during the day of April 21st, 2008. Note that in both cases, temperatures increase at night and decrease during the day due to the total aerosol effect.

While much has been speculated about the role of anthropogenic black carbon in Arctic warming, this study shows that the aerosol semi-direct effect is almost negligible due to low black carbon concentration. The aerosol direct effect contributes a small cooling by scattering incoming solar radiation. The temperature changes that occur over land and sea ice are dominated by aerosol indirect effects, whereby an increase in fine mode aerosols results in an increase in cloud optical depth. This increased cloudiness has two effects on the radiation balance at the surface: an increase in downward longwave radiation that is proportional to the increase in cloud optical depth, and a decrease in downward shortwave radiation that is proportional to both the increase in cloud optical depth and the amount of solar insolation.

The aerosol indirect effects have both a warming effect and a cooling effect, depending upon the time of day and surface type. At night, there is no solar insolation, and hence no decrease in downward shortwave radiation. As a result, the increase in downward longwave radiation dominates and results in a warming of surface temperature at night. Over sea ice, a strong night-time surface temperature warming is the result of a high fine mode aerosol concentration, which leads to an increase in cloud optical depth and a strong increase in

Table 4.1: Summary of aerosol effects on surface temperature

	Land		Sea Ice	
	Day	Night	Day	Night
Direct Effect Impact	Low	Negligible	Low	Negligible
Semi-Direct Effect Impact	Negligible	Negligible	Negligible	Negligible
Indirect Effects Impact	High	Low	Low	High
Cloud Optical Depth Impact	High	Low	Low	High
Downward Shortwave Impact	High	Negligible	High	Negligible
Downward Longwave Impact	Low	Low	Low	High
Effect on Surface Temperature	Strong Cooling	Weak Warming	Weak Cooling	Strong Warming

downward longwave radiation. Over land, a weak night-time surface temperature warming is the result of a high coarse aerosol concentration, which leads to an increase in precipitation, a decrease in cloud optical depth, and a decrease in downward longwave radiation. In addition, stronger upward longwave radiation over land surfaces tends to diminish the warming effect of downward longwave radiation.

During the day, the decrease in downward shortwave radiation dominates the increase in downward longwave radiation, resulting in surface temperature cooling. Over sea ice, a weak day-time surface temperature cooling is the result of a modest increase in cloud optical depth and a relatively weak solar insolation compared to lower latitudes. Over land, a strong day-time surface temperature cooling is the result of an abundance of moisture and aerosols, an increase in cloud depth, and a strong solar insolation compared to higher latitudes. The effects of aerosols on the diurnal cycle of Arctic surface temperature is summarized in Table 4.1.

4.2 Future Work

There are many ways in which future work may be of some utility to the scientific community. One way in which the project could be expanded would be to look at aerosol effects in other seasons. Because the diurnal cycle changes drastically throughout the year, a simulation spanning the entire year would enable the study of these large changes on the surface temperature. Another way in which this study could be enhanced is to explore the effects that aerosols have on ice particles. At the moment, this is not taken into account in most models (including WRF-CHEM). This will have large implications for the lifetime of Arctic stratiform clouds, which are highly influenced by the Wegener-Bergeron-Findeisen process.

Appendix A: Alternate Temperature Readings

It may be of interest to see how the surface temperature is handled at several observation stations throughout the domain. The four observation stations are: Barrow, a site on the northern coast of Alaska, Fairbanks, a site in the Alaskan interior with a relatively low altitude, Kodiak, a site in the Aleutian Islands (near the area of cloud changes), and Yakutat, on the coast of the Gulf of Alaska and near to another area of cloud changes. Figure A.1 shows the surface temperature for the Control Run, the NoChem run, and the station observation at each time step for 4 stations on the top portion of the plot (note that the 2 meter temperature was used to match the observational value). The bottom portion of each panel shows the difference in surface temperature between the Control Run and the NoChem run for that station as a function of time for the analysis period. The Barrow plot shows that the Control Run is the same or slightly cooler than the NoChem run for all time points except for the early morning hours of April 20th, wherein the Control Run is 4 degrees higher than the NoChem run. It should be noted that the Control Run has a warm bias of similar strength against the observation at this point. The Fairbanks plot shows that the Control Run is generally cooler than the NoChem run at the surface. However, both the Control Run and the NoChem run seem to miss the strength of the diurnal cycle that is shown in observations. At Kodiak, the Control Run again seems to be cooler than the NoChem run, with both runs doing a reasonable job in simulating the observed diurnal cycle. Yakutat shows some significant cooling, and is the point most strongly affected by the large aerosol and cloud differences in the Gulf of Alaska, though again neither run seems to capture the extent of the diurnal cycle.

Another way in which the temperature may be explored is to examine the time height profile through meteograms at specific points, namely the observation stations that have been shown before. Figure A.2 shows the time height meteograms for the Barrow, Fairbanks, Kodiak, and Yakutat stations. In the top portion of each panel, the plot shows the

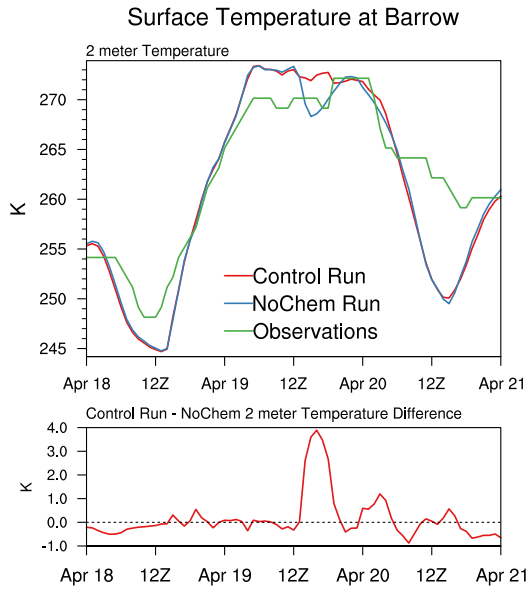

(a) Surface Temperature at Barrow

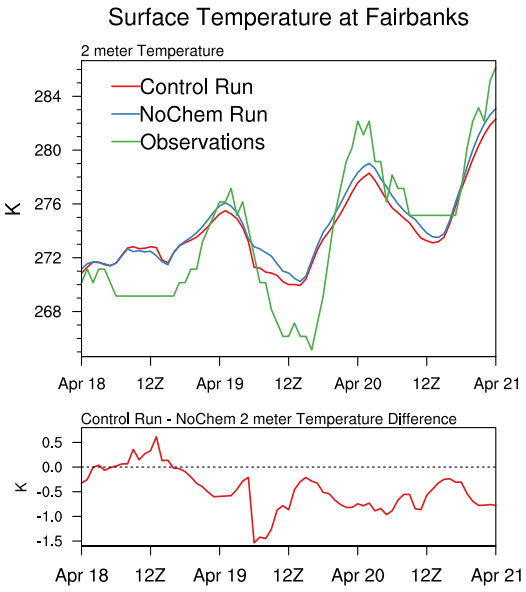

(b) Surface Temperature at Fairbanks

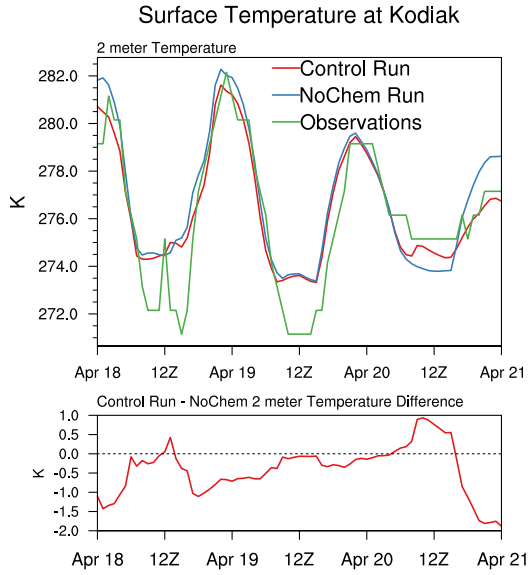

(c) Surface Temperature at Kodiak

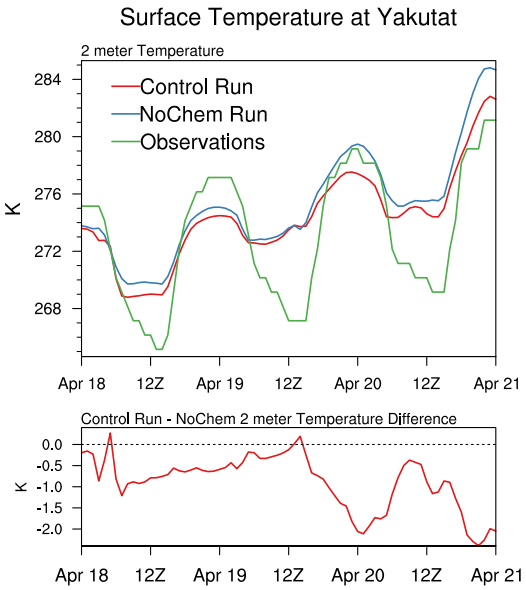

(d) Surface Temperature at Yakutat

Figure A.1: The four panels show the 2 meter Surface Temperature at a given Observation Station. The top portion of the panel shows the Control Run Surface Temperature in red, the NoChem run Surface Temperature in blue, and the Observation Surface Temperature in green. The bottom portion of the panel shows the Control Run - NoChem run difference in Surface Temperature. The plots are shown for the following stations: a) Barrow, b) Fairbanks, c) Kodiak, d) Yakutat

vertical profile of temperature at the station across each time step. The bottom portion of the panel shows the same plot, except instead of the vertical profile of temperature, the plots show the vertical profile of the temperature differences between the Control Run and the NoChem run. This will allow an examination of where exactly in the profile aerosols are making their impact. The Barrow plot shows that a warm front is passing through the area during the analysis period. However, there is significant cooling (up to 4K) at the 850mb level then compared to the NoChem run. This suggests that aerosols are increasing the boundary layer in this area, as the profile in the Control Run lends itself to more vertical mixing. Fairbanks also experiences a mild temperature increase during the analysis period. When compared to the NoChem run, Fairbanks also shows cooling, especially right at the surface around April 19th, 06Z. This was also shown in the plot of surface temperature differences for Fairbanks. As with Barrow, this profile would lend itself to increased boundary layer heights. Kodiak appears to show an overall cooling trend at the surface throughout the analysis period, as a cold front moves in. The very start of the analysis period shows that there is an increase in temperature at the 850mb level, but a decrease right below it. This suggests stronger vertical mixing below an inversion at 850mb. Since this station is in the area of increased cloud formation in the Aleutian islands, it seems reasonable to conclude that the profile induced by the aerosols has led to even stronger cloud development. Yakutat shows a generally flat surface temperature profile with a slight increase towards the end of the analysis period. The Control Run - NoChem differences show that there is increased cooling at the surface (or rather, that the Control Run is not heating up as fast as the NoChem run). This may be due to the large cloud and aerosol presence just off the coast from Yakutat in the Gulf of Alaska.

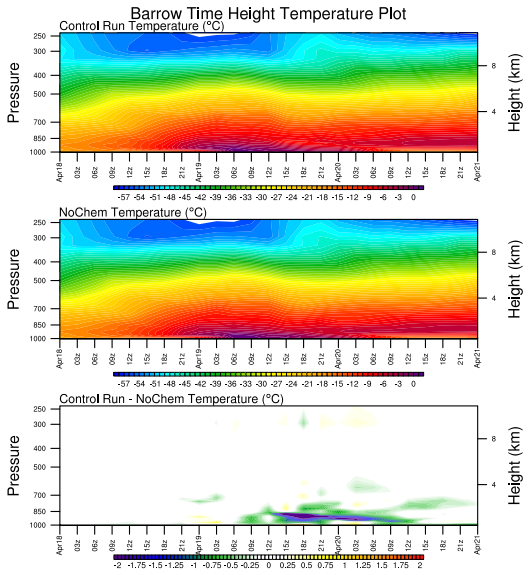

(a) Time Height Meteogram at Barrow

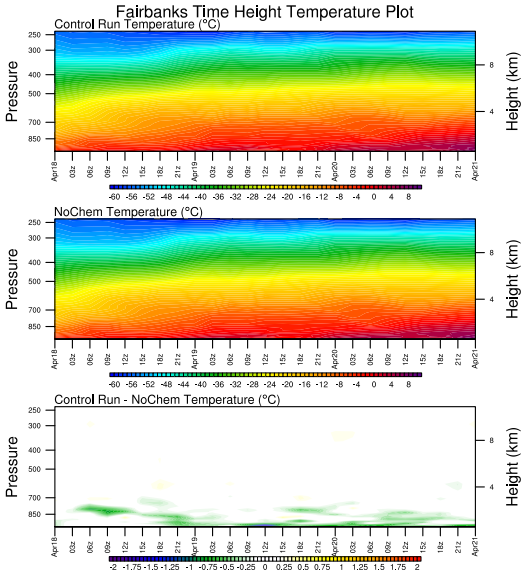

(b) Time Height Meteogram at Fairbanks

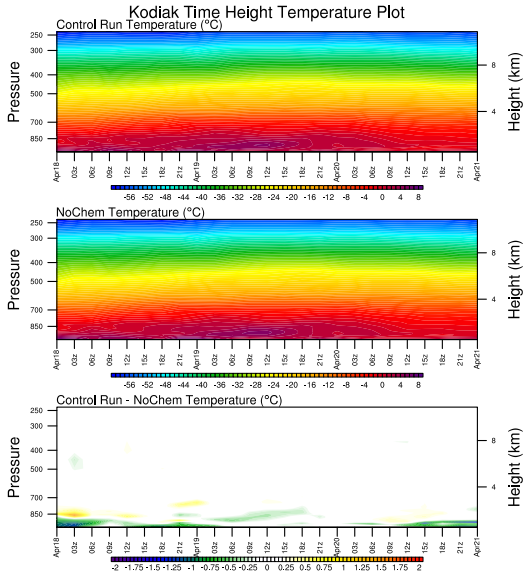

(c) Time Height Meteogram at Kodiak

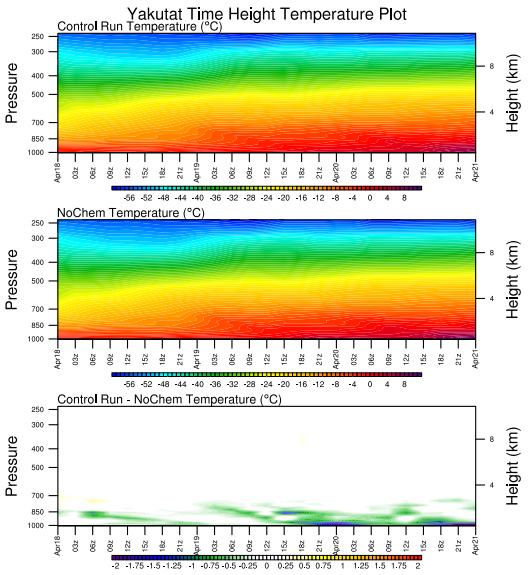

(d) Time Height Meteogram at Yakutat

Figure A.2: The four panels show the Time Height plot of Temperature at a given Observation Station. The top portion of the panel shows the Control Run Temperature Profile over the analysis period. The bottom portion of the panel shows the Control Run - NoChem run difference in the Temperature Profile over the analysis period. The plots are shown for the following stations: a) Barrow, b) Fairbanks, c) Kodiak, d) Yakutat

Bibliography

Albrecht, B., 1989: Aerosols, cloud microphysics and fractional cloudiness. *Science*, **245**, 1227–1230.

Alexeev, V. A., P. L. Langen, and J. R. Bates, 2005: Polar amplification of surface warming on an aquaplanet in ghost forcing experiments without sea ice feedbacks. *Clim. Dyn.*, **24 (7-8)**, 655–666.

Anderson, J. L. and W. F. Stern, 1995: Evaluating the potential predictive utility of ensemble forecasts. *J. Climate*, **9**, 260–269.

Bond, T., E. Bhardwaj, R. Dong, R. Jogani, S. Jung, C. Roden, D. Streets, and N. Trautmann, 2007: Historical emissions of black carbon and organic carbon aerosol from energy-related combustion, 1850-2000. *Global Biogeochem. Cycles*, **21**, 2018–2018.

Boucher, O., D. Randall, P. Artaxo, C. Bretherton, G. Feingold, P. Forster, V. Kerminen, Y. Kondo, H. Liao, U. Lohmann, P. Rasch, S. K. Satheesh, S. Sherwood, B. Stevens, and X. Y. Zhang, 2013: Clouds and Aerosols. In: *Climate Change 2013: The Physical Science Basis. Contribution of Working Group I to the Fifth Assessment Report of the Intergovernmental Panel on Climate Change* [Stocker, T. F., D. Qin, G. Plattner, M. Tignor, S. K. Allen, J. Boschung, A. Nauels, Y. Xia, V. Bex, and P. M. Midgley (eds.)]. Cambridge University Press, Cambridge, United Kingdom and New York, NY, USA.

Boybeyi, Z., N. N. Ahmad, D. P. Bacon, T. J. Dunn, M. S. Hall, P. C. S. Lee, R. A. Sarma, and T. R. Wait, 2000: Evaluation of the Operational Multi-scale Environment model

with Grid Adaptivity against the European Tracer Experiment. *J. Appl. Meteor.*, **40**, 1541–1558.

Browse, J., K. S. Carslaw, G. W. Mann, C. E. Birch, S. R. Arnold, and C. Leck, 2014: The complex response of Arctic aerosol to sea-ice retreat. *Atmos. Chem. Phys.*, **14**, 7543–7557.

Chang, J. C. and S. R. Hanna, 2004: Air quality model performance evaluation. *Meteor. Atmos. Phys.*, **87**, 167–196.

Chang, J. C., S. R. Hanna, Z. Boybeyi, and P. Franzese, 2005: Use of Salt Lake City Urban 2000 field data to evaluate the urban Hazard Prediction Assesment Capability (HPAC) Dispersion model. *J. Appl. Meteor.*, **44**, 485–501.

Christensen, J. H., K. Krishna Kumar, E. Aldrian, S. An, I. F. A. Cavalcanti, M. de Castro, W. Dong, P. Goswami, A. Hall, J. K. Kanyanga, A. Kitoh, J. Kossin, N. Lau, J. Renwick, D. B. Stephenson, S. Xie, and T. Zhou, 2013: Climate Phenomena and their Relevance for Future Regional Climate Change. In: *Climate Change 2013: The Physical Science Basis. Contribution of Working Group I to the Fifth Assessment Report of the Intergovernmental Panel on Climate Change* [Stocker, T. F., D. Qin, G. Plattner, M. Tignor, S. K. Allen, J. Boschung, A. Nauels, Y. Xia, V. Bex, and P. M. Midgley (eds.)]. Cambridge University Press, Cambridge, United Kingdom and New York, NY, USA.

Collins, M., R. Knutti, J. Arblaster, J. Dufresne, T. Fichefet, P. Friedlingstein, X. Gao, W. J. Gutowski, T. Johns, G. Krinner, M. Shongwe, C. Tebaldi, A. J. Weaver, and M. Wehner, 2013: Long-term Climate Change: Projections, Commitments and Irreversibility. In: *Climate Change 2013: The Physical Science Basis. Contribution of Working Group I to the Fifth Assessment Report of the Intergovernmental Panel on Climate Change* [Stocker, T. F., D. Qin, G. Plattner, M. Tignor, S. K. Allen, J. Boschung, A. Nauels, Y. Xia, V. Bex, and P. M. Midgley (eds.)]. Cambridge University Press, Cambridge, United Kingdom and New York, NY, USA.

Cubasch, U., D. Wuebbles, D. Chen, M. C. Facchini, D. Frame, N. Mahowald, and

J. Winther, 2013: Introduction. In: *Climate Change 2013: The Physical Science Basis. Contribution of Working Group I to the Fifth Assessment Report of the Intergovernmental Panel on Climate Change* [Stocker, T. F., D. Qin, G. Plattner, M. Tignor, S. K. Allen, J. Boschung, A. Nauels, Y. Xia, V. Bex, and P. M. Midgley (eds.)]. Cambridge University Press, Cambridge, United Kingdom and New York, NY, USA.

de Boer, G., H. Morrison, M. D. Shupe, and R. Hildner, 2011: Evidence of liquid dependent ice nucleation in high-latitude stratiform clouds from surface remote sensors. *Geophys. Res. Lett.*, **38 (1)**.

de Winter, J. C. F., 2013: Using the students t-test with extremely small sample sizes. *Pract. assess., res. eval.*, **18**.

Fast, J., et al., 2009: Evaluating simulated primary anthropogenic and biomass burning organic aerosols during milagro: implications for assessing treatments of secondary organic aerosols. *Atmos. Chem. Phys.*, **9 (16)**, 6191–6215.

Flato, G., J. Marotzke, B. Abiodun, P. Braconnot, S. C. Chou, W. Collins, P. Cox, F. Driouech, S. Emori, V. Eyring, C. Forest, P. Gleckler, E. Guilyardi, C. Jakob, V. Kattsov, C. Reason, and M. Rummukainen, 2013: Evaluation of Climate Models. In: *Climate Change 2013: The Physical Science Basis. Contribution of Working Group I to the Fifth Assessment Report of the Intergovernmental Panel on Climate Change* [Stocker, T. F., D. Qin, G. Plattner, M. Tignor, S. K. Allen, J. Boschung, A. Nauels, Y. Xia, V. Bex, and P. M. Midgley (eds.)]. Cambridge University Press, Cambridge, United Kingdom and New York, NY, USA.

Garrett, T. J. and C. Zhao, 2006: Increased arctic cloud longwave emissivity associated with pollution from mid-latitudes. *Nature*, **440 (7085)**, 787–789, doi:10.1038/nature04636, URL http://dx.doi.org/10.1038/nature04636.

Girard, E. and J.-P. Blanchet, 2001: Simulation of Arctic Diamond Dust, Ice Fog, and Thin Stratus Using an Explicit AerosolCloudRadiation Model. *J. Atmos. Sci.*, **58**, 1199–1221.

Girard, E., J.-P. Blanchet, and Y. Dubois, 2005: Effects of arctic sulphuric acid aerosols on wintertime low-level atmospheric ice crystals, humidity and temperature at alert, nunavut. *Atmos. Res.*, **73 (12)**, 131–148.

Grell, G., S. Peckham, R. Schmitz, S. McKeen, G. Frost, W. Skamarock, and B. Eder, 2005: Fully coupled online chemistry within the WRF model. *Atm. Env.*, **39**, 6957–6975.

Hamill, T. M., 1999: Hypothesis tests for evaluating numerical precipitation forecasts. *Wea. Forecasting*, **14**, 155–167.

Hanna, S. R. and R. Yang, 2001: Evaluation of mesoscale models' simulations of near-surface winds, tempearture gradients, and mixing heights. *J. Appl. Meteor.*, **40**, 1095–1104.

Hansen, J., M. Sato, and R. Ruedy, 1997: Radiative forcing and climate response. *J. Geophys. Res.*, **102**, 6831–6864.

Hartmann, D. L., A. M. G. Klein Tank, M. Rusticucci, L. V. Alexander, S. Brönnimann, Y. Charabi, F. J. Dentener, E. J. Dlugokencky, D. R. Easterling, A. Kaplan, B. J. Soden, P. W. Thorne, M. Wild, and P. M. Zhai, 2013: Observations: Atmosphere and Surface. In: *Climate Change 2013: The Physical Science Basis. Contribution of Working Group I to the Fifth Assessment Report of the Intergovernmental Panel on Climate Change* [Stocker, T. F., D. Qin, G. Plattner, M. Tignor, S. K. Allen, J. Boschung, A. Nauels, Y. Xia, V. Bex, and P. M. Midgley (eds.)]. Cambridge University Press, Cambridge, United Kingdom and New York, NY, USA.

Haywood, J. M. and O. Boucher, 2000: Estimates of the direct and indirect radiative forcings due to tropospheric aerosols: A Review. *Rev. Geophys.*, **38**, 513–543.

Houghton, J. T., Y. Ding, D. J. Griggs, M. Noguer, P. J. van der Linden, X. Dai, K. Maskell, and C. A. Johnson, 2001: Contribution of working group I to the Third Assessment Report of the Intergovernmental Panel on Climate Change. Tech. rep., Cambridge University Press.

Koch, D., S. Menon, A. Del Genio, R. Ruedy, I. Alienov, and G. A. Schmidt, 2009: Distinguishing Aerosol Impacts on Climate over the Past Century. *J. Climate*, **22**, 2659–2677.

Kogan, Y. L., D. B. Mechem, and K. Choi, 2011: Effects of sea-salt aerosols on precipitation in simulations of shallow cumulus. *J. Atmos. Sci.*, **69 (2)**, 463–483.

Korolev, A., 2007: Limitations of the Wegener-Bergeron-Findeisen mechanism in the evolution of mixed-phase clouds. *J. Atmos. Sci.*, **64 (9)**, 3372–3375.

Lin, Y.-L., R. D. Farley, and H. D. Orville, 1983: Bulk Parameterization of the Snow Field in a Cloud Model. *J. Appl. Meteor.*, **22**, 1065–1092.

Lindeman, J., Z. Boybeyi, and I. Gultepe, 2011: An examination of the aerosol semi-direct for a polluted case of the ISDAC field campaign. *J. Geophys. Res.*, **116 (D1)**.

Lohmann, U. and G. Lesins, 2002: Stronger constraints on the anthropogenic indirect aerosol effect. *Science*, **298**, 1012–1016.

Morrison, H., G. de Boer, G. Feingold, J. Harrington, M. D. Shupe, and K. Sulia, 2012: Resilience of persistent arctic mixed-phase clouds. *Nat. Geosci.*, **5 (1)**, 11–17.

Myhre, G., D. Shindell, F. Bron, W. Collins, J. Fuglestvedt, J. Huang, D. Koch, J. Lamarque, D. Lee, B. Mendoza, T. Nakajima, A. Robock, G. Stephens, T. Takemura, and H. Zhang, 2013: Anthropogenic and Natural Radiative Forcing. In: *Climate Change 2013: The Physical Science Basis. Contribution of Working Group I to the Fifth Assessment Report of the Intergovernmental Panel on Climate Change* [Stocker, T. F., D. Qin, G. Plattner, M. Tignor, S. K. Allen, J. Boschung, A. Nauels, Y. Xia, V. Bex, and P. M. Midgley (eds.)]. Cambridge University Press, Cambridge, United Kingdom and New York, NY, USA.

Ovchinnikov, M., A. Korolev, and J. Fan, 2011: Effects of ice number concentration on dynamics of a shallow mixed-phase stratiform cloud. *J. Geophys. Res.: Atmos.*, **116 (D1)**.

Rosenfeld, D., 1999: TRMM observed first direct evidence of smoke from forest fires inhibiting rainfall. *Geophys. Res. Lett.*, **26**, 3105–3108.

Skamarock, W. C., J. Klemp, J. Dudhia, D. Gill, D. Barker, M. Duda, X. Huang, W. Wang, and J. Powers, 2008: A description of the advanced research WRF version 3. Tech. rep., NCAR.

Solomon, S., D. Qin, M. Manning, Z. Chen, M. Marquis, K. B. Averyt, M. Tignor, and H. L. Miller, 2007: *Contribution of Working Group I to the Fourth Assessment Report of the Intergovernmental Panel on Climate Change*. Cambridge University Press, URL http://www.ipcc.ch/ipccreports/ar4-wg1.htm.

Twomey, S. A., 1977: The influence of pollution on the shortwave albedo of clouds. *J. Atmos. Sci.*, **34**, 1149–1152.

Vaughan, D. G., J. C. Comiso, I. Allison, J. Carrasco, G. Kaser, R. Kwok, P. Mote, T. Murray, F. Paul, J. Ren, E. Rignot, O. Solomina, K. Steffen, and T. Zhang, 2013: Observations: Cryosphere. In: *Climate Change 2013: The Physical Science Basis. Contribution of Working Group I to the Fifth Assessment Report of the Intergovernmental Panel on Climate Change* [Stocker, T. F., D. Qin, G. Plattner, M. Tignor, S. K. Allen, J. Boschung, A. Nauels, Y. Xia, V. Bex, and P. M. Midgley (eds.)]. Cambridge University Press, Cambridge, United Kingdom and New York, NY, USA.

Wilks, D. S., 1995: *Statistical methods in the atmospheric sciences: an introduction*. Academic Press, San Diego.

Zaveri, R. A., R. C. Easter, J. D. Fast, and L. K. Peters, 2008: Model for simulating aerosol interactions and chemistry (MOSAIC). *J. Geophys. Res.*, **113 (D13)**, D13 204+.

Biography

Eric Stofferahn was born and raised in Springfield, Virginia. He attended James Madison University, where he received his Bachelor of Science in Physics in 2005. He went on to receive his Master of Science in Earth Systems Science from George Mason University in 2008. He then received his Doctorate in Climate Dynamics from George Mason University in 2015.